Chapter 6

Tautomerization of tropolone

6.1 Introduction

This Chapter addresses the application of the techniques discussed in the foregoing Chapter 5. In particular, the construction of the Cartesian Reaction Plane (CRP) Hamiltonian is demonstrated for the HAT in the electronic ground state of tropolone [TRN(OH)]. TRN is a prototype system for HAT (similar to malonaldehyde). The tautomerization reaction of tropolone is depicted in Fig. 6.1a. The minimum geometries have C_s symmetry while the transition state (not shown) has C_{2v} symmetry. The two equivalent minima are interconverted by the permutation P which permutes C_1 and C_2, C_3 and C_7, C_4 and C_6, O_8 and O_9 as well as corresponding hydrogens (cf. Section 2.2.1). Moreover, the Hamiltonian is invariant with respect to space inversion I^*, where I denotes the identity. The symmetry group G_4 [10] with operations $\{I, P, I^*, P^*\}$, where $P^* = P\,I^*$, is isomorphous to C_{2v}, i.e., there are four one-dimensional irreducible representations, A_1, A_2, B_1, and B_2 [10, 11, 40]. Eigenstates can either be gerade (+1) or ungerade (-1) with respect to P and they can either be in-plane (+1) or out-of-plane (-1) corresponding

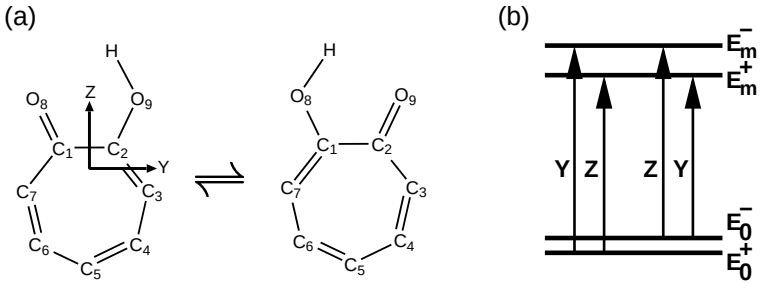

Figure 6.1: (a) Tautomerization reaction of tropolone [TRN(OH)]. Minimum geometries are interconverted by the permutation P (cf. Section 2.2.1). (b) Allowed in-plane IR transitions; responsible dipole components are indicated.

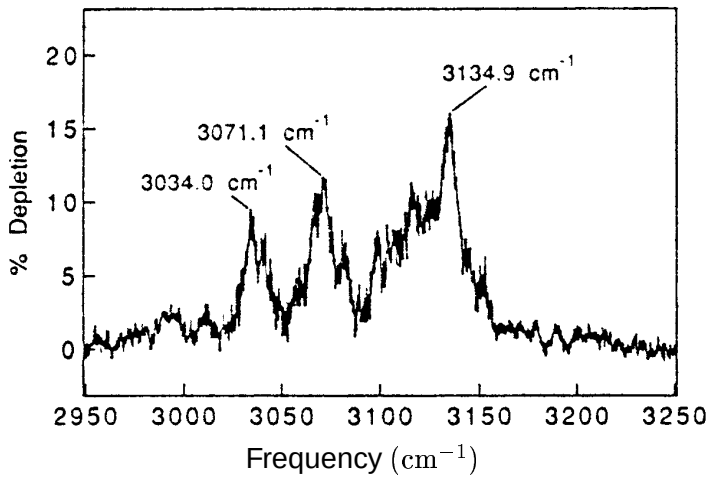

Figure 6.2: Fluoresence-dip IR spectrum of the OH stretch region of jet-cooled TRN(OH) for transitions out of the gerade ground state level [159].

to the transformation with respect to I^*. For the fundamental transitions one finds that in-plane states have either A_1 or B_2 symmetry, and out-of-plane states have either A_2 or B_1 symmetry [40, 159]. There are 27 in-plane and 12 out-of-plane normal mode vibrations. The four possible ground state $\rightarrow$ excited state IR transitions for the in-plane modes are shown in Fig. 6.1b, they follow from the fact that Y and Z transform according to B_2 and A_1, respectively [11]. The X coordinate transforms according to B_1 [11]. Thus, for the out-of-plane modes, group theory allows only for transitions from the gerade ground state (A_1) into an ungerade out-of-plane fundamental (B_1), and transitions from the ungerade ground state (B_2) into a gerade out-of-plane fundamental (A_2), since $B_1 \times B_2 = A_2$. The tunneling splitting between gerade and ungerade vibrational eigenstates is mode-specific (cf. Section 2.2.2). Experimentally, this was first observed for the electronically first excited state S_1 [155, 156, 157, 158].

The electronic ground state S_0 was investigated experimentally with high spectral resolution [160, 159, 48, 40]. Tanaka *et al.* [160] measured the ground state tunneling splitting of gaseous TRN(OH) by microwave spectroscopy and found $\Delta_0^{(\exp)}[\mathrm{TRN(OH)}] = 0.974\ cm^{-1}$. Concerning the interpretation of the OH stretch region (cf. Fig. 6.2) there is a controversy in the literature: Frost *et al.* [159] performed fluoresence-dip IR measurements and assigned the most intense peak at $3134.9\ \mathrm{cm}^{-1}$ to be the OH stretch fundamental transition corresponding to the gerade initial state and suggested that the peak with opposite symmetry lies within unresolved absorption around $12\ \mathrm{cm}^{-1}$ to the red. Redington *et al.* [48] assigned the OH stretch doublet to be at $3102\ \mathrm{cm}^{-1}$ and $3121\ \mathrm{cm}^{-1}$, respectively; therefore, the tunneling splitting is $\Delta_1 \approx 20\ \mathrm{cm}^{-1}$. The intense

Method	Ref.	$E_{\ddagger}(\mathrm{kJ/mol})$	$E_{\ddagger}/hc\,(\mathrm{cm}^{-1})$
B3LYP/6-31+G(d)	[114]	25.9	2161
B3LYP/6-31+G(d,p)		21.3	1778
G3(MP2)$^{(a)}$	[114]	30.1	2518
$^{(b)}$	[114]	32.2	2693
MP2$^{(c)}$	[40]	15.1	1271
MP4(SDQ)$^{(c,d)}$	[40]	29.3	2448

$^{(a)}$ Ref. [162]; $^{(b)}$ multicoeffi cient correlation method; details see Ref. [163]; $^{(c)}$ 6-311G(df,pd) for the $COH\cdots OC$ fragment, and 6-311G(d,p) for the rest; $^{(d)}$ MP2 geometry

Table 6.1: Comparison of barrier heights obtained by different quantum chemistry methods for tropolone [TRN(OH)].

peak at $3134.9\ \mathrm{cm}^{-1}$ was attributed to a combination state transition. The assignment was based on IR spectra obtained from vapor phase, solvated, and rare-gas matrix-isolated samples of TRN(OH) and the deuterated species TRN(OD) and on the measurements of Frost *et al.* [159]. In particular, an assigment of modes was given guided by quantum chemistry calculations. The assignment is therefore partly based on the harmonic approximation.

Several theoretical investigations of the electronic ground [75, 148, 161, 47] and fi rst excited state [76, 75, 148] were carried out. For instance, Vener *et al.* [148] studied the HAT in terms of a 3D *ab-initio* PES in which only the $O\cdots H-O$ fragment was considered. Tautermann *et al.* [114] determined the ground state tunneling splitting in terms of the approximate instanton approach (cf. Section 3.1.3) to be $0.75\,\Delta_0^{(\mathrm{exp})}$. Redington [47] emphasized the importance of *heavy atom tunneling*, i.e., the HAT is accompanied by a contortion of the molecular skeleton. The issue was addressed in terms of an empirical model [47] (cf. also Section 6.2.1).

From the theoretical view point another fi nding requires attention. The barrier obtained by the present level of quantum chemistry [B3LYP/6-31G(d)] (cf. Chapter 5) is $2161\ cm^{-1}$ [114]. Table 6.1 shows barrier heights obtained by various different quantum chemical methods. Tentatively, the barrier is therefore well below $3000\ \mathrm{cm}^{-1}$. The inclusion of ZPE effects usually leads to a decreasing barrier, because modes at the saddle point weaken. Thus, any IR transition into the OH stretch according to the experimental assignment would be above the barrier.

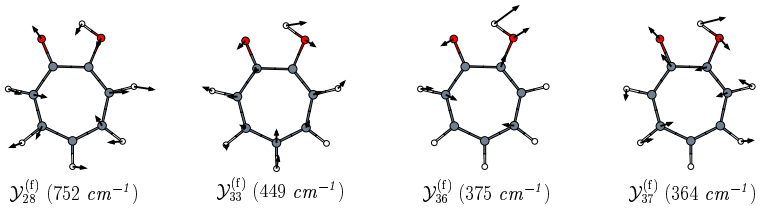

Figure 6.3: Selected full normal modes of TRN(OH) (cf. Tab. 6.2). Normal mode frequencies are indicated.

6.2 A Cartesian reaction plane Hamiltonian for tropolone

6.2.1 Intrinsic reaction path analysis

The IRP is a well-known means to characterize a chemical reaction [67] (cf. Sections 2.2.1, 3.1.3, and 5.1.1), but in general a chemical reaction does not necessarily proceed along the IRP [164]. However, for *tunneling* in the semiclassical limit $\hbar \to 0$ the least action principle leads to usually one dominating trajectory (cf. Sections 3.1.2 and 3.1.3) that generally differs from the IRP, e.g., due to corner cutting. The least action principle was successfully applied to various HAT systems [108, 114, 126], among them tropolone [114]: the theoretical value obtained by applying the least action principle to the GT paths (cf. Section 3.1.3) yielded $0.75\,\Delta_0^{(\mathrm{exp})}$. The GT paths [cf. Eq. (3.11)] are a two-dimensional superposition of the direct tunneling direction [cf. Eq. (3.22)] and the IRP. In Section 5.1.2 the differences between the IRP $\mathbf{X}(s)$ and its projection $\bar{\mathbf{X}}(s)$ were discussed for the special case of TRN(OH) and TRN(OD); the maximum root mean squared atom displacement was found to be less than 0.025 Å for both species (cf. Fig. 5.3) and the maximum energy difference along the paths was less than $120\,\mathrm{cm}^{-1}$ and $100\,\mathrm{cm}^{-1}$ for, respectively, TRN(OH) and TRN(OD). This leads to the conclusion that the IRP lies approximately in the reaction plane for the considered molecules.

Table 6.3 shows frequencies of all full normal modes (FNM) $\mathcal{Y}_k^{(\mathrm{f})}$ together with their IR intensities for TRN(OH). FNM are introduced in Section 5.2.2. Recall, FNM correspond to the diagonalization of the full-dimensional Hessian at the (right) minimum geometry. The normal modes are ordered by decreasing value of the the corresponding normal mode frequency (different notation than in Refs. [48, 40, 47].) Based on an empirical model, Redington *et al.* [48, 40, 47] assigned a particular normal mode, that is, $\mathcal{Y}_{28}^{(\mathrm{f})}$ (in the present notation; cf. Fig. 6.3) at about $750\ cm^{-1}$ to be the nascent tautomerization coordinate. This assignment

TRN(OH)						
in-plane				out-of-plane		
no.	$\omega_k^{(\mathrm{f})}/2\pi c$	Inten.	δ	no.	$\omega_k^{(\mathrm{f})}/2\pi c$	Inten.
1	3329	134	36	20	1030	1.2
2	3198	8.6	0	21	1013	0.3
3	3193	14.9	0	23	946	11.0
4	3186	12.0	0	25	878	10.6
5	3171	4.1	0	26	816	77.0
6	3163	6.5	0	27	772	79.9
7	1675	202	14	29	723	17.9
8	1664	2.8	7	31	597	0.3
9	1617	105	19	34	402	1.8
10	1540	124	19	35	376	0.0
11	1523	142	16	38	185	0.0
12	1480	212	26	39	115	1.05
13	1454	26.9	11			
14	1349	57.9	4			
15	1327	227	39			
16	1294	39.4	12			
17	1249	8.6	9			
18	1245	7.5	11			
19	1080	0.4	11			
22	977	10.2	7			
24	888	10.9	3			
28	752	14.5	22			
30	694	7.2	21			
32	546	1.8	19			
33	449	15.2	33			
36	375	5.3	45			
37	364	5.2	44			

Table 6.2: Normal mode frequencies (in cm^{-1}) and IR intensities "Inten." (in km/mol) for TRN(OH) [B3LYP/6-31+G(d)]. The dimensionless parameter δ [cf. Eq. (6.2)] measures the change of the hydrogen bond geometry. (Obtained by Gaussian 03 [152].) The normal modes $\mathcal{Y}_k^{(\mathrm{f})}$ are labeled in decreasing order of their frequency. Modes no. 1, 15, and 26 are the OH stretch, OH bend, and OH out-of-plane mode, respectively.

was motivated by the statement that mode no. 28 most closely suggests entrance into the valley of the IRP. No numerical evidence was given for that statement and it is not in accord with the stable limit theorem (cf. Section 2.2.1), since the weakest in-plane mode $\mathcal{Y}_{37}^{(\mathrm{f})}$ is at $364\ \mathrm{cm}^{-1}$ (cf. Fig. 6.3). Moreover, by inspecting the displacements of right localized full normal modes along the IRP (s is the IRC),

$$\Delta\mathcal{Y}_k^{(\mathrm{f})}(s) = (\mathbf{X}(s) - \mathbf{X}_R) \cdot \boldsymbol{\mathcal{Y}}_k^{(\mathrm{f})}, \tag{6.1}$$

one finds largest displacements for the modes $\mathcal{Y}_{33}^{(\mathrm{f})}$, $\mathcal{Y}_{36}^{(\mathrm{f})}$, and $\mathcal{Y}_{37}^{(\mathrm{f})}$ (cf. Fig. 6.3). For instance, $\max|\Delta\mathcal{Y}_{36}^{(\mathrm{f})}| = 0.90\ \ a_0\ amu^{1/2}$, whereas $\max|\Delta\mathcal{Y}_{28}^{(\mathrm{f})}| = 0.08\ \ a_0\ amu^{1/2}$ for mode 28. Thus, for mode no. 28, neither significant displacement along the IRP nor significant contribution when the IRP approaches the minimum can be found.

The change of the hydrogen bond geometry that is induced by a certain normal mode can be quantified by the dimensionless value

$$\delta = |\delta r_{O_1-O_2}| + |\delta r_{H_1-O_1}| + |\delta r_{H_1-O_2}|, \tag{6.2}$$

where $r_{\mathrm{bond}}(\mathbf{X})$ is the bond length of the specified bond in geometry $\mathbf{X}$ and δr_{bond} is defined as the derivative

$$\delta r_{\mathrm{bond}} = \left.\frac{\mathrm{d}r_{\mathrm{bond}}(\mathbf{X}_R + h \cdot \boldsymbol{\mathcal{Y}}_k^{(\mathrm{f})})}{\mathrm{d}h}\right|_{h=0}, \tag{6.3}$$

with a normal mode vector $\boldsymbol{\mathcal{Y}}_k^{(\mathrm{f})}$. That is, δr_{bond} is the change of a special bond length induced by motion along that mode in the vicinity of the right minimum geometry $\mathbf{X}_R$.

The dimensionless δ-values are also given for the in-plane modes in Tab. 6.2; for the out-of-plane modes δ vanishes. Mode $\mathcal{Y}_{28}^{(\mathrm{f})}$ is not among the modes with largest influence on the hydrogen bond geometry. Instead, the two in-plane modes with lowest frequency, mode no. 36 and 37, have the largest δ-values.

There is a near degeneracy of modes $\mathcal{Y}_{36}^{(\mathrm{f})}$ ($375\ \ cm^{-1}$) and $\mathcal{Y}_{37}^{(\mathrm{f})}$ ($364\ \ cm^{-1}$), thus the interplay between full normal modes no. 36 and 37 in the vicinity of the (right) minimum has to be analyzed carefully if one aims to obtain deeper insight into the tautomerization coordinates: In the upper panel of the left column of Fig. 6.4 a cut of the full potential U of TRN(OH) along the normal mode directions $\mathcal{Y}_{36}^{(\mathrm{f})}$ and $\mathcal{Y}_{37}^{(\mathrm{f})}$ is shown. The potential was obtained by Shepard interpolation; this was discussed already in Sec. 5.1.2. The influence of mode no. 33 with a somewhat larger frequency of $449\ \ cm^{-1}$ is not considered, since a mixing of energetically close modes is more likely. A projection of the IRP onto the two modes is also shown (thick curve). In the scale of the viewgraph, the IRP is only slightly curved

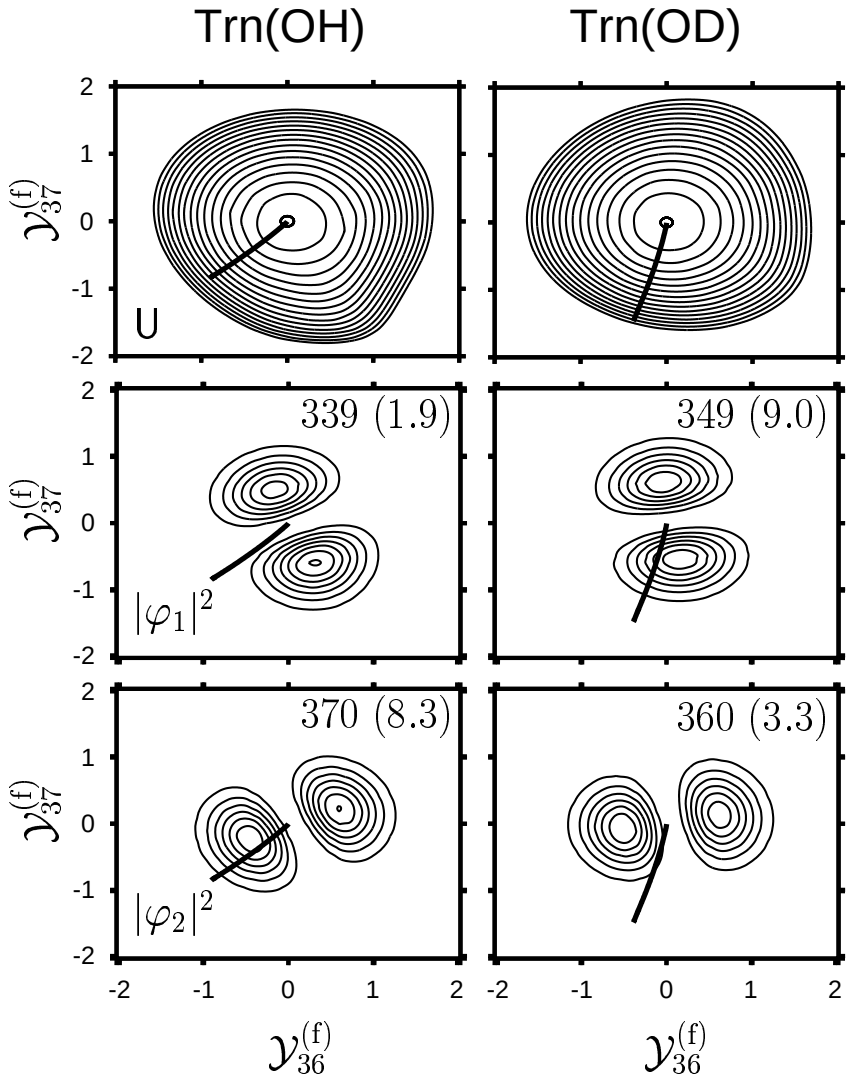

Figure 6.4: Comparison of Trn(OH) and Trn(OD) [B3LYP/6-31+G(d)]. *Upper row:* Contour plot of the potential U for a cut along the full normal mode directions $\mathcal{Y}_{36}^{(f)}$ and $\mathcal{Y}_{37}^{(f)}$ (units $a_0\, amu^{1/2}$). The contour line spacing is $100\ cm^{-1}$ and the maximum contour line is at $1500\ cm^{-1}$. The projection of the IRP is given as thick lines. *Middle and Bottom row:* Contour plot of densities of the first and second excited states, respectively, with respect to the 2D potential U. Frequencies (in cm^{-1}) and IR intensities (parenthesized; in km/mol) are given in the figures. (Improved relaxation [26] on a 51×51 sine-DVR grid.)

towards the weakest mode. This is a consequence of the near degeneracy of the two weakest in-plane modes.

The first φ_1 and second φ_2 excited state with respect to the 2D PES U for TRN(OH) are shown in the middle and bottom panel of the left column of Fig. 6.4. For a harmonic PES, the two excited states would be directed, respectively, along the $\mathcal{Y}_{36}^{(\mathrm{f})}$ and $\mathcal{Y}_{37}^{(\mathrm{f})}$ axis. However, the calculation unveils, that the eigenstates are tilted in a way such that the second excited one is directed along the IRP (thick curve), while the first excited one, is almost orthogonal to the IRP. The frequency difference is increased as compared to the harmonic modes, but - more importantly - the tilting of the wave functions drastically changes the IR intensities: while for the harmonic modes both IR intensities are about $5\ \mathrm{km/mol}$, the IR intensity of the state φ_2 directed along the IRP is about 4 times larger than that for the orthogonal state φ_1, i.e., IR intensity is enhanced for a vibration in direction of the IRP. Since the IRP lies approximately in the reaction plane, so does the vibrational direction corresponding to state φ_2.

The deuterated species, TRN(OD), is considered in the right column of Fig. 6.4 (selected normal mode frequencies are given in Tab. 6.5). For this species, the harmonic frequencies of mode no. 36 ($369\ cm^{-1}$) and 37 ($352\ cm^{-1}$) show a small isotope effect. The frequency difference is slightly decreased for the anharmonic case (values given in Fig. 6.4) as compared to the harmonic case. The projected IRP (thick curve) is more strongly tilted towards the lowest frequency mode no. 37 as compared to the protonated species. Note, the difference of harmonic frequencies is increased in TRN(OD) as compared to TRN(OH). The correlation between IRP direction and vibrational direction of the wave function is less pronounced compared to TRN(OH). The lowest state has a larger overlap with the IRP curve than the second excited state. Again, vibration along the IRP enhances the IR intensity.

Two observations are important: (i) the "competition" between the nearly degenerated modes no. 36 and 37 is decided such that one mode (not necessarily the lowest one) is tilted towards the IRP, and (ii) the spacial extent of the considered low frequency modes is of the same order of magnitude as the maximum displacements of normal modes no. 36 and 37 along the IRP. (Recall, that these modes are among the modes with largest displacement along the IRP.) The finding suggests that excitation of the modes that are tilted towards the IRP will show a pronounced enhancement of the tunneling splitting upon excitation. These modes are referred to as *reaction modes* in the following. The almost orthogonal modes are considered to be less relevant for the tautomerization process.

6.2.2 Mode selection

The goal of this Section is the construction of a model of TRN(OH) with reduced dimensionality (reduced model) based on the CRP approach (cf. Chapter 5). In particular, the choice of relevant modes (cf. Sec. 5.2.2) is discussed. Recall, the CRP-Hamiltonian of a reduced model depends on model coordinates $(w_1, w_2, q_1, \ldots, q_n)$, where (w_1, w_2) are the reaction plane coordinates and n is the number of relevant modes q_j. The relevant modes are orthogonal to the reaction plane and a certain relevant mode is either symmetric or anti-symmetric with respect to the molecular symmetry transformation T. Recall, T is the combination of the permutation of atoms P (cf. Section 6.1) and a rotation such that the two symmetrically related minima are connected by a rotation free path (cf. Sec. 2.2.1).

A normal mode analysis of the reduced model with respect to, say, the right minimum, $(w_1^{(\min)}, w_2^{(\min)}, \mathbf{q} = 0)$, yields $n+2$ unique *reduced normal modes* (RNM) $\mathcal{Y}_k^{(n+2)}$ with corresponding $n+2$ reduced normal mode vectors $\boldsymbol{\mathcal{Y}}_k^{(n+2)}$ of dimension $n+2$ (cf. Sec. 5.2.2). This is analogous to the full-dimensional case, for which there are $N-6$ *full normal modes* (FNM) $\mathcal{Y}_k^{(\mathrm{f})}$ with corresponding N-dimensional full normal mode vectors $\boldsymbol{\mathcal{Y}}_k^{(\mathrm{f})}$. It is important to note that RNM and model coordinates *span the same configuration space*, i.e., these coordinates are linear combinations of each other. The RNM are unqiuely defi ned by diagonalizing the Hessian at the (right) minimum, while the model coordinates are convenient for expressing the CRP Hamiltonian.

In the following, it is assumed that the OH stretch region is dominated by various Fermi resonances with overtone and combination states. This is suggested by previous experimental work [48]. Fermi resonances may be described within perturbation theory. The states corresponding to the harmonic approximation with respect to one minimum serve as zero-order (or unperturbed) states $\Psi_j^{(0)}$ with energy $E_j^{(0)}$, where j accounts for the collection of all quantum numbers. First-order perturbation theory states, that the expansion of the new OH stretch level $\Psi_1^{(1)}$ in terms of the old levels reads (without normalization),

$$\Psi_1^{(1)} = \Psi_1^{(0)} + \sum_{j=2}^{\infty} c_j \, \Psi_j^{(0)}, \quad c_j = \frac{\langle \Psi_j^{(0)} | \hat{H} | \Psi_1^{(0)} \rangle}{E_1^{(0)} - E_j^{(0)}}. \tag{6.4}$$

A state $\Psi_j^{(0)}$ corresponds to the fundamental, overtone, or combination excitation of certain mode(s). Thus, a large expansion coeffi cient c_j indicates the relevance of the underlying mode(s).

The coupling matrix element vanishes for states with an odd number of excited out-of-plane modes due to symmetry. This includes binary combinations of in-plane and out-of-plane fundamentals with one quantum per mode. For other

normal mode	overlaps								
	symmetric					anti-symmetric			
	Q_4	Q_5	Q_6	Q_7	Q_8	Q_{23}	Q_{24}	Q_{25}	Q_{26}
$\mathcal{Y}_1^{(\mathrm{f})}$	**0.61**								
$\mathcal{Y}_7^{(\mathrm{f})}$	0.30	**0.87**							
$\mathcal{Y}_8^{(\mathrm{f})}$			0.42			**0.75**	0.34		
$\mathcal{Y}_9^{(\mathrm{f})}$		0.31	**0.63**	0.28		0.49			
$\mathcal{Y}_{10}^{(\mathrm{f})}$						0.26	0.53	**0.68**	
$\mathcal{Y}_{11}^{(\mathrm{f})}$			0.31	0.35	0.33		**0.68**	0.32	
$\mathcal{Y}_{12}^{(\mathrm{f})}$	0.38		0.41	0.29	**0.63**			0.29	
$\mathcal{Y}_{13}^{(\mathrm{f})}$				0.46				0.47	**0.70**

Table 6.3: Overlap [Eq. (6.5)] of selected full normal modes (FNM) and Q_j-modes. The Q_j-modes are either symmetric or anti-symmetric with respect to the molecular symmetry transformation T (see text). Only overlaps > 0.25 are shown for clarity. Modes with largest overlap are included in the model and are marked by bold-face numbers.

states, the evaluation of the coupling matrix element c_j requires the knowledge of the full-dimensional Hamiltonian $\hat{H}$. The corresponding cumbersome computations of high-dimensional matrix elements hamper a direct use of c_j as order parameter for the mode relevance. To proceed, consider all those states with energy in a $\pm\, 200\ \mathrm{cm}^{-1}$ range around the harmonic OH stretch at $3329\ \mathrm{cm}^{-1}$. This range is motivated by the width of the experimental OH stretch band (vapor phase) [48, 159].

All out-of-plane modes and some in-plane modes are excluded by this choice. The CH stretch modes $\mathcal{Y}_2^{(\mathrm{f})}, \ldots, \mathcal{Y}_6^{(\mathrm{f})}$ correspond to fundamentals in the considered energy range. However, the CH stretch modes are linear combinations of local CH stretch modes and do not have any signifi cant influence on the $CO - H \cdots OC$ fragment (vanishing δ-values in Tab. 6.2). For that reason, irrespective of the small denominator of c_j, the CH stretch modes are considered to be non-relevant for the description of the OH stretch coupling.

Several combination states corresponding to the modes $\mathcal{Y}_7^{(\mathrm{f})}, \ldots, \mathcal{Y}_{13}^{(\mathrm{f})}$ reside in the considered energy range. These modes were also considered by Redington *et al.* [48] for the interpretation of the OH stretch region in terms of combination transitions of observed IR transitions in the range $1400 - 1700\,\mathrm{cm}^{-1}$. Therefore, there should be RNM that closely resemble the FNM, i.e., the overlap [cf. Eq. (5.36)] of certain pairs of RNM and FNM should be close to one.

In Section 5.2.1 the space that is orthogonal to the reaction plane (i.e., the

space of *all possible* relevant modes) was expressed in terms of eigenvectors $\mathbf{e}_k$ of the projected transition state Hessian Eq. (5.7). The corresponding coordinates were labeled Q_k. A necessary condition for the overlap Eq. (5.36) beeing large for certain RNM/FNM pairs is that the projection of the FNM into the space spanned by the model coordinates (the reduced space) is large. (Recall, all RNM span the same space as the model coordinates.) Thus it is reasonable to consider overlaps of FNM and the vectors $\mathbf{e}_k$,

$$\tilde{p}_{jk} = \boldsymbol{\mathcal{Y}}_j^{(\mathrm{f})} \cdot \mathbf{e}_k. \tag{6.5}$$

The modes Q_k are labeled in the order of decreasing eigenvalues; the symmetric modes are $\{Q_1, \ldots, Q_{20}\}$ and the the anti-symmetric modes are $\{Q_{21}, \ldots, Q_{37}\}$. The overlap of the FNM no. 7 to 13 and the OH stretch mode $\mathcal{Y}_1^{(\mathrm{f})}$ with the Q_j-modes is shown in Tab. 6.3. Modes with largest overlap are included in the model and are marked by bold-face numbers. (For the OH stretch FNM no. 1, all Q_j-overlaps are also shown in Fig. 6.6a.)

Additionally to the modes discussed so far, the full normal mode $\mathcal{Y}_{30}^{(\mathrm{f})}$ is also taken into account, because its energy is very close to the first overtone of the reaction mode (see below). A rather small coupling may lead to a mixing of these states due their near resonance. Moreover, mode $\mathcal{Y}_{28}^{(\mathrm{f})}$ is included in order to check the assignment of Redington *et al.* (cf. Section 6.1). The overlap of mode $\mathcal{Y}_{28}^{(\mathrm{f})}$ and $\mathcal{Y}_{30}^{(\mathrm{f})}$ is largest with Q-mode Q_{32} (anti-symmetric, overlap 0.96) and Q_{16} (symmetric, overlap 0.97), respectively.

The preceding discussion leads to a 12D model with relevant mode vector,

$$\mathbf{q}^{[\mathrm{12D,TRN(OH)}]} := (Q_4, Q_5, Q_6, Q_8, Q_{16}, Q_{23}, Q_{24}, Q_{25}, Q_{26}, Q_{32})^t. \tag{6.6}$$

Thus, the vector of model coordinates is 12D and reads $(w_1, w_2, \mathbf{q}^{[\mathrm{12D,TRN(OH)}]})$. The ZPE term [fourth term on the r.h.s. of Eq. (5.31)] corresponding to the spectator modes lowers the barrier by $134\,\mathrm{cm}^{-1}$. Note, this term only includes the ZPE of modes that are not included directly into the model.

The 12 reduced normal modes (RNM) of the model are shown in Fig. 6.5; Table 6.4 shows overlaps with full normal modes (FNM) and overlaps with the directions of the reaction plane, $\mathbf{w}_1$ and $\mathbf{w}_2$ [cf. Eqs. (3.22-3.23)]. There are three RNM, $\mathcal{Y}_1^{(\mathrm{12D})}$, $\mathcal{Y}_9^{(\mathrm{12D})}$, $\mathcal{Y}_{12}^{(\mathrm{12D})}$, with a comparatively large overlap with the reaction plane (cf. 7th and 8th column of Tab. 6.4). RNM $\mathcal{Y}_1^{(\mathrm{12D})}$ almost coincides with the OH stretch FNM $\mathcal{Y}_1^{(\mathrm{f})}$ (overlap 0.97; 4th column of Tab. 6.4). The small residual overlap with other modes leads to a decrease of the RNM frequency by $102\,\mathrm{cm}^{-1}$ (-3 %). RNM $\mathcal{Y}_9^{(\mathrm{12D})}$ has a significant overlap with FNM $\mathcal{Y}_{15}^{(\mathrm{f})}$ (overlap 0.72), which has OH bend character and shows the largest IR intensity. This FNM is considered to be the "nominal" OH bend [48]. RNM $\mathcal{Y}_{12}^{(\mathrm{12D})}$ has lowest frequency and shows significant overlaps with FNM $\mathcal{Y}_{33}^{(\mathrm{f})}$, $\mathcal{Y}_{36}^{(\mathrm{f})}$, and $\mathcal{Y}_{37}^{(\mathrm{f})}$. This

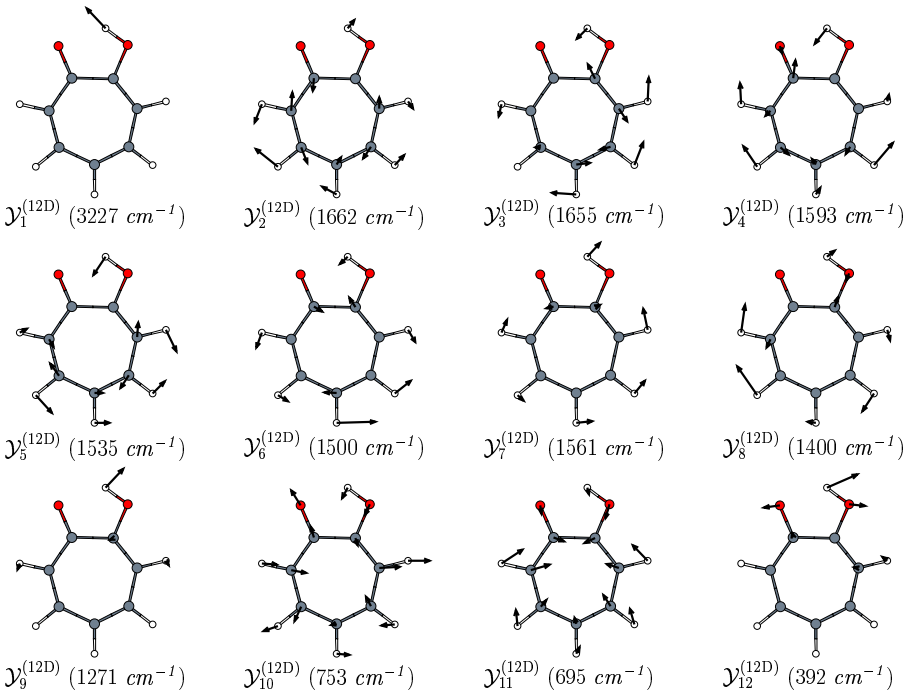

Figure 6.5: The reduced normal modes of the 12D model of TRN(OH). Frequencies are indicated.

full			12D				
no.	$\omega_k^{(\mathrm{f})}/2\pi c$	Inten.	overlap	mode	$\omega_k^{(\mathrm{12D})}/2\pi c$	w_1	w_2
1	3329	133.7	0.97	$\mathcal{Y}_1^{(\mathrm{12D})}$	3227	-0.64	0.31
7	1674	202.4	0.87	$\mathcal{Y}_2^{(\mathrm{12D})}$	1662	-0.01	0.00
8	1663	2.82	0.89	$\mathcal{Y}_3^{(\mathrm{12D})}$	1655	-0.15	0.04
9	1617	104.6	0.91	$\mathcal{Y}_4^{(\mathrm{12D})}$	1593	0.06	-0.01
10	1539	124.5	0.94	$\mathcal{Y}_5^{(\mathrm{12D})}$	1535	0.04	0.00
11	1522	141.9	0.85	$\mathcal{Y}_6^{(\mathrm{12D})}$	1500	-0.26	0.07
12	1480	212.0	0.83	$\mathcal{Y}_7^{(\mathrm{12D})}$	1461	0.17	-0.07
13	1454	27.0	0.59	$\mathcal{Y}_8^{(\mathrm{12D})}$	1400	-0.04	0.00
14	1349	57.7	0.65				
15	1327	227.5	0.72	$\mathcal{Y}_9^{(\mathrm{12D})}$	1271	0.60	-0.11
28	752	14.5	1.00	$\mathcal{Y}_{10}^{(\mathrm{12D})}$	753	-0.11	0.03
30	694	7.2	1.00	$\mathcal{Y}_{11}^{(\mathrm{12D})}$	695	-0.03	0.00
33	449	15.2	0.41				
36	375	5.3	0.70	$\mathcal{Y}_{12}^{(\mathrm{12D})}$	392	0.32	0.94
37	364	5.2	0.56				

Table 6.4: Comparison of normal modes of the full-dimensional system ("full") with the reduced normal modes of the 12D model ("12D") for TRN(OH). Frequencies ω_k (in cm^{-1}), IR intensities ("Inten.", in km/mol), overlaps of the reduced normal modes with full normal modes [cf. Eq. (5.36)], and overlaps of the reduced normal modes with the reaction plane directions, $|\mathbf{w}_1 \cdot \boldsymbol{\mathcal{Y}}_k^{(12D)}|$ ("w_1") and $|\mathbf{w}_2 \cdot \boldsymbol{\mathcal{Y}}_k^{(12D)}|$ ("w_2"), are given.

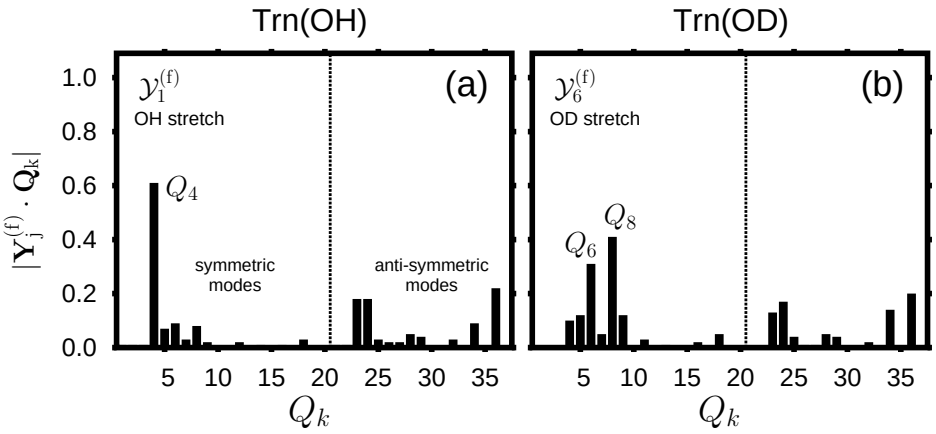

Figure 6.6: Overlaps of the OH/OD stretch full normal mode (FNM) with Q_k-modes for TRN(OH) and TRN(OD), respectively. The OH stretch FNM $\mathcal{Y}_1^{(\mathrm{f})}$ has large overlap with Q_4; the OD stretch FNM $\mathcal{Y}_1^{(\mathrm{f})}$ has large overlaps with Q_6 and Q_8. The large overlaps motivates the inclusion of these modes in the respective models.

RNM is reminicent of the findings of Section 6.2.1; tentatively it is called the *reaction mode* of the 12D model.

Reaction plane overlaps of the remaining RNM are markedly smaller. Most modes have a clear FNM counterpart (overlaps > 0.83) and the RNM frequencies are only slightly changed; due to the reduced dimensionality, RNM no. 8 has significant overlap with two FNM, however. Modes $\mathcal{Y}_{10}^{(12D)}$ and $\mathcal{Y}_{11}^{(12D)}$ coincide with the corresponding FNM $\mathcal{Y}_{28}^{(\mathrm{f})}$ and $\mathcal{Y}_{30}^{(\mathrm{f})}$, respectively. Moreover, these modes almost coincide with the model coordinates $q_{10} \equiv Q_{32}$ (anti-symmetric) and $q_5 \equiv Q_{16}$ (symmetric).

The 12D model of TRN(OH) was choosen according to resonance conditions, which will change for the deuterated species TRN(OD). A comparison of isotope effects concerning the OH/OD stretch is not attempted here. Instead the isotope effect concerning low lying energy levels (e.g., ground state tunneling splittings) is studied by discarding the FNM no. 7 to 13 and FNM no. 30. Thus, a 4D model is considered with relevant mode vector

$$\mathbf{q}^{[4\mathrm{D},\mathrm{TRN(OH)}]} := (Q_4, Q_{32})^t. \tag{6.7}$$

The ZPE term [cf. Eq. (5.31)] lowers the barrier by $148\,\mathrm{cm}^{-1}$, which is an insignificant change compared to the 12D model. The RNM are labeled $\mathcal{Y}_1^{(4D)}$ to $\mathcal{Y}_4^{(4D)}$. These modes correspond, respectively, to the OH stretch, OH bend, nascent tautomerization coordinate (according to Redington *et al.*), and reaction mode. The main difference as compared to the 12D model concerning the above discussion is: (i) the OH stretch overlap is 0.92 with RNM frequency decreased

full			4D				
no.	$\omega_k^{(\mathrm{f})}/2\pi c$	Inten.	overlap	mode	$\omega_k^{(12\mathrm{D})}/2\pi c$	w_1	w_2
6	2421	81.8	0.92	$\mathcal{Y}_1^{(4\mathrm{D})}$	2269	0.69	0.42
18	1121	43.9	0.37				
21	1002	22.2	0.63	$\mathcal{Y}_2^{(4\mathrm{D})}$	1074	0.55	0.20
22	967	41.0	0.43				
27	748	12.1	0.96	$\mathcal{Y}_3^{(4\mathrm{D})}$	757	0.09	0.07
33	442	13.6	0.30				
36	369	2.1	0.29	$\mathcal{Y}_4^{(4\mathrm{D})}$	389	0.46	0.88
37	352	10.7	0.89				

Table 6.5: Same as Tab. 6.4, but for the 4D model of TRN(OD).

to $3113\,\mathrm{cm}^{-1}$, and (ii) the OH bend overlap with FNM no. 15 is reduced to only 0.44 with RNM frequency $1366\,\mathrm{cm}^{-1}$. Frequencies of the remaining RNM, $\mathcal{Y}_3^{(4D)}$ and $\mathcal{Y}_4^{(4D)}$, are $743\,\mathrm{cm}^{-1}$ and $406\,\mathrm{cm}^{-1}$, respectively.

The corresponding 4D model of the deuterated species, TRN(OD), involves a different choice of relevant modes. This is illustrated in Fig. 6.6, where overlaps of the OH/OD stretch FNM are shown for both species. For TRN(OH) only one Q_j-modes is selected (cf. previous discussion in this Section). (Note, different symmetries are not allowed to be mixed.) For TRN(OD) the OD stretch is dominated by two mode overlaps. Furthermore, like in the case of TRN(OH), the nascent tautomerization coordinate of TRN(OD) (FNM no. 27) has a large overlap of 0.94 with the anti-symmetric mode Q_{26}. This motivates to use the relevant mode vector,

$$\mathbf{q}^{[4\mathrm{D,TRN(OD)}]} := (2^{-1/2}\,\{Q_6 + Q_8\}, Q_{26})^t, \tag{6.8}$$

for the 4D model of TRN(OD). Recall, that one is free to choose linear combinations of Q_j-modes [cf. Eq. (5.18)] with same symmetry. A more refined linear combination does not lead to a refined model, because of the limited dimensionality. (Left out modes have similar magnitudes of overlaps as the difference of the magnitudes of the largest overlaps.) The ZPE term [cf. Eq. (5.31)] lowers the barrier by $302\,\mathrm{cm}^{-1}$. The four RNM (no. 1 to no. 4) correspond, respectively, to the OH stretch, OH bend, nascent tautomerization coordinate, and reaction mode. Properties of the reduced and full dimensional harmonic modes are compared in Tab. 6.5. In particular, the RNM $\mathcal{Y}_4^{(4D)}$ has a large overlap with the weakest in plane FNM $\mathcal{Y}_{37}^{(\mathrm{f})}$, which is reminiscent of the right column of Fig. 6.4.

6.2.3 The IR spectrum: low lying states

This Section addresses the state-specific tunneling splittings of states below $800\,\mathrm{cm}^{-1}$. The splittings are of the order of 1 to $10\,\mathrm{cm}^{-1}$, i.e., an accurate determination method is required. However, a direct diagonalization of the 12D Hamiltonian (e.g., by the Lanczos method) is not feasible. An alternative method is introduced that is based on a combination of improved relaxation (cf. Section 2.3.1) and diagonalization with a reduced basis set. The remaining spectrum - including the OH stretch band - is obtained with lower accuracy by Fourier transformation of an appropriate dipole-dipole auto-correlation function in Section 6.2.4.

In principle it is possible to obtain ground and excited states directly by the MCTDH approach with improved relaxation (cf. Section 2.3.1). However, experience shows that the relaxation leads to a localization of the states in one of the minima, i.e., the states relax to a superposition of gerade and ungerade states. To overcome this problem a symmetrization/anti-symmetrization procedure of SPF was implemented in the MCTDH package [140]. Unfortunately such procedure is not applicable, when anti-symmetric modes are present, because SPF of both symmetries are necessary to describe the full-dimensional wave function. To this end, a method is presented that uses localized states as non-orthogonal basis for the diagonalization of the Hamiltonian.

The states $\Psi_{\mathbf{n}}^{(0,R)}$ ($\Psi_{\mathbf{n}}^{(0,L)}$) corresponding to the harmonic approximation to the right (left) minimum serve as initial states for MCTDH improved relaxations (cf. Section 2.3.1). The relaxations yield new relaxed states $\Psi_{\mathbf{n}}^{(\mathrm{rel},R)}$ and $\Psi_{\mathbf{n}}^{(\mathrm{rel},L)}$, respectively. These states form an optimized basis for the diagonalization of the Hamiltonian. The left and right states are not orthogonal, thus eigenstates and eigenvectors of the Hamiltonian can be obtained by solving the generalized eigenvalue problem,

$$\sum_{\mathbf{n}'} \sum_{\sigma'=R,L} \left(H_{\mathbf{n},\mathbf{n}'}^{\sigma,\sigma'} - \varepsilon_l \, S_{\mathbf{n},\mathbf{n}'}^{\sigma,\sigma'} \right) \cdot c_{\mathbf{n}',l}^{\sigma'} = 0, \tag{6.9}$$

where $\sigma = R$ or L, $H_{\mathbf{n},\mathbf{n}'}^{\sigma,\sigma'} = \langle \Psi_{\mathbf{n}}^{(\mathrm{rel},\sigma)} | \hat{H} | \Psi_{\mathbf{n}'}^{(\mathrm{rel},\sigma')} \rangle$ is the Hamiltonian matrix, $S_{\mathbf{n},\mathbf{n}'}^{\sigma,\sigma'} = \langle \Psi_{\mathbf{n}}^{(\mathrm{rel},\sigma)} | \Psi_{\mathbf{n}'}^{(\mathrm{rel},\sigma')} \rangle$ is the overlap matrix, and $c_{\mathbf{n}',l}^{\sigma'}$ are the expansion coefficients for the eigenstate no. l,

$$\Psi_l^{(12D)} = \sum_{\mathbf{n}} \sum_{\sigma=R,L} c_{\mathbf{n},l}^{\sigma} \Psi_{\mathbf{n}}^{(\mathrm{rel},\sigma)}, \tag{6.10}$$

with eigenenergy ε_l. The present procedure requires less single particle functions than the attempt to compute the gerade and ungerade states directly by improved relaxation.

Table 6.6 shows the primitive basis and the mode combinations that were used for the improved relaxation. The number of SPF for the combined modes c_1 to

no.	coord.	n	$q_{min}^{(a)}$	$q_{max}^{(a)}$	comb.
1	w_1	31	-3.0	3.0	c_1
2	w_2	31	-2.0	4.0	c_1
3	q_1	19	-1.5	1.5	c_2
4	q_2	19	-1.5	1.5	c_2
5	q_3	19	-1.5	1.5	c_3
6	q_4	19	-1.5	1.5	c_3
7	q_5	19	-1.5	1.5	c_4
8	q_6	19	-1.5	1.5	c_4
9	q_7	19	-1.5	1.5	c_5
10	q_8	19	-1.5	1.5	c_5
11	q_9	19	-2.0	2.0	c_6
12	q_{10}	19	-2.0	2.0	c_6

(a) in $a_0\, amu^{1/2}$

Table 6.6: Primitive basis and mode combinations (indicated by indentical c_j's) used for the MCTDH calculations (cf. Sec. 2.3.1). The sine-DVR representation was used, where the grid extends from q_{min} to q_{max} with n grid points.

state	T (fs)	$\lvert\Delta E\rvert(\mathrm{cm}^{-1})$	crit. pop.
gs	16	0.01	$1.2 \cdot 10^{-4}$
10^1	20	0.01	$2.9 \cdot 10^{-4}$
11^1	8	0.05	$3.9 \cdot 10^{-4}$
12^1	8	0.1	$2.0 \cdot 10^{-4}$
12^2	8	0.5	$2.3 \cdot 10^{-4}$

Table 6.7: Parameters for MCTDH improved relaxation. The 10 relaxed states $\Psi_{\mathbf{n}}^{(\mathrm{rel,R/L})}$ with $\mathbf{n} = gs, 10, 11, 12, 12^2$ (see text) were used as basis for solving Eq. (6.9). T is the relaxation time, ΔE is the energy change for the last relaxation step, and "crit. pop." is the maximum critical population.

c_6 are 6 / 6 / 4 / 4 / 4 / 4. All 10 right and left harmonic states below $800\ \mathrm{cm}^{-1}$ were included; for completeness Table 6.7 shows the used relaxation time, energy convergence, and critical population of each individual state. The relaxed states are perturbed harmonic oscillator states. The labeling scheme is n^k, where $\mathcal{Y}_n^{(12D)}$ is the corresponding harmonic mode and k is the number of quanta in that mode. The ground state is labeled as "gs"; combined states do not appear below $800\,\mathrm{cm}^{-1}$. The basis is symmetry adapted; gerade and ungerade superpositions can be formed,

$$\Psi_{\mathbf{n}}^{(\mathrm{rel},\pm)} \propto \Psi_{\mathbf{n}}^{(\mathrm{rel,R})} \pm \Psi_{\mathbf{n}}^{(\mathrm{rel,L})}, \tag{6.11}$$

with appropriate normalization.

A ground state tunneling splitting of $\Delta_0 = 2.7\,\mathrm{cm}^{-1}$ was found by solving Eq. (6.9) with the present basis of 10 relaxed states. In order to check the accuracy (and as a prerequisite for Section 6.2.4) the gerade and ungerade ground state were also determined by performing the improved relaxation directly for these states. The initial states were constructed by using the gerade and ungerade eigenstate of an appropriate 1D Hamiltonian for the w_1 DOF. The states were converged to $\Delta E < 0.003\,\mathrm{cm}^{-1}$. The tunneling splittings was found to be $\Delta_0 = 3.4\,\mathrm{cm}^{-1}$ and the energy of the gerade ground state obtained by direct improved relaxation was $3.3\,\mathrm{cm}^{-1}$ *higher* than the energy of the state obtained by relaxing $\Psi_{\mathrm{gs}}^{(\mathrm{rel,R})}$. The reason for this small deviation is that the present diagonalization method would correspond to a direct improved relaxation with twice as many SPF per anti-symmetric DOF.

Compared to the experimental tunneling splitting, $\Delta_0^{(\mathrm{exp})} = 0.974\,\mathrm{cm}^{-1}$ [160], the present result is about 3 times too large. Two errors contribute to this overestimation: (i) results of Ref. [114] suggest the barrier to be about $360 - 530\,\mathrm{cm}^{-1}$ higher and (ii) the inclusion of out-of-plane modes typically decreases the tunneling splitting (cf. Section 2.2.3). Recently, the last issue was demonstrated for malonaldehyde [165].

The results (i.e., eigenenergies and IR intensities) of the diagonalization procedure are shown in Table 6.8 (indicated as "H-12"). The symmetry of the states is either gerade ("+") or ungerade ("-"). The labeling of states is $n\ ^k_{\pm}$, where n is the RNM number and k is the number of quanta in that mode (cf. also Tab. 6.7). The Eigenenergies are given with respect to the gerade ground state level Ψ_{gs}^{+}. A pronounced mode selectivity is found for the states 12^k corresponding to mode $\mathcal{Y}_{12}^{(12D)}$: the splitting increases to $14\,\mathrm{cm}^{-1}$ for the fundamental (12^1) and to $41\,\mathrm{cm}^{-1}$ for the first overtone (12^2). According to Section 6.2.2, this mode most closely resembles the reaction mode, i.e., that mode, that vibrates in the direction of the IRP. The magnitude of the splitting of the remaining states is almost unchanged compared to Δ_0. The order of the gerade/ungerade levels of states $10^1_{\pm}$

final state Ψ_f	ϵ_j/hc (cm^{-1})			IR Intensity ($\mathrm{km/mol}$)					
				$\Psi_0^+ \rightarrow \Psi_f$			$\Psi_0^- \rightarrow \Psi_f$		
	H-12	H-4	D-4	H-12	H-4	D-4	H-12	H-4	D-4
$12_+^1\,(4_+^1)$	357	354	363	7.1	6.7	4.1	14.0	10.6	5.9
$12_-^1\,(4_-^1)$	371	372	364	8.8	5.2	5.6	6.2	6.4	4.0
$12_+^2\,(4_+^2)$	697	690	728	0.6	0.6	1.0	0.7	0.9	0.2
$12_-^2\,(4_-^2)$	737	744	737	0.0	0.1	0.1	0.5	0.3	0.7
11_+^1	696			0.2			6.0		
11_-^1	699			6.4			0.2		
$10_+^1\,(3_+^1)$	752	752	756	0.7	1.7	3.3	14.6	20.7	21.3
$10_-^1\,(3_-^1)$	750	749	757	15.6	21.5	12.3	0.6	1.1	3.3

Table 6.8: Excitation energies (ε_j) and IR intensities for the 12D model of TRN(OH) ["H-12"], for the 4D model of TRN(OH) ["H-4"], and for the 4D model of TRN(OD) ["D-4"]. The labeling of states is $n\,{}_{\pm}^{k}$, where n is the RNM number and k is the number of quanta in that mode and $\pm$ specifies the symmetry; parenthesized values refer to the 4D models. The ground state tunneling splittings are: $2.7\,\mathrm{cm}^{-1}$ (H-12), $3.5\,\mathrm{cm}^{-1}$ (H-4), and $0.16\,\mathrm{cm}^{-1}$ (D-4).

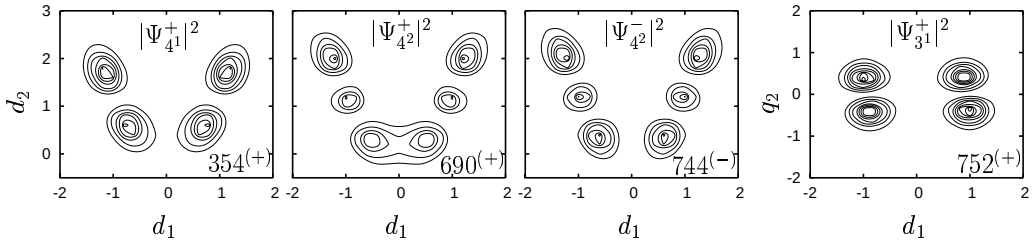

Figure 6.7: Densities $|\Psi|^2$ of selected states of the 4D model of TRN(OH). The transition frequency (in cm^{-1}) and the symmetry ($\pm$) is indicated. The states were obtained by energy screening. (Note, there are different y-axis labels.)

are reversed. Mode $\mathcal{Y}_{10}^{(12D)}$ almost coincides with model coordinate $q_{10} \equiv Q_{32}$; this model coordinate shows anti-symmetric coupling. For excited states of modes with anti-symmetric coupling the order of gerade/ungerade states can be reversed (cf. Section 2.2.3) [57].

IR transitions can be characterized to be of one of the four types: gerade-gerade ($g \to g$), gerade-ungerade ($g \to u$), ungerade-gerade ($u \to g$), and ungerade-ungerade ($u \to u$). All four possible types of IR transitions are symmetrically allowed for in-plane fundamentals (cf. Fig. 6.1). For transitions into the states $10^1_\pm$ (corresponding to the nascent tautomerization coordinate) and $11^1_\pm$, the intensity for the $g \to u$ and $u \to g$ transitions is significantly larger than for the $g \to g$ and $u \to u$ transitions, i.e., the Z transition dipole is significantly weaker than the Y transition dipole [40]. On the opposite, all possible transitions into the states $12^1_\pm$ have significant intensity. This indicates that these states are more strongly perturbed compared to the corresponding harmonic states. The intensity for transitions into the overtone states $12^2_\pm$ is weak. In particular, there is no Fermi resonance between the very close lying states 12^2_+ and 11^1_+. Recall that the investigation of this possibility was the reason for treating mode $\mathcal{Y}_{11}^{(\mathrm{f})}$ as relevant.

Table 6.8 also shows results for the 4D models of TRN(OH) and TRN(OD) [cf. Section 6.2.2]. These values were obtained by Lanczos diagonalization, i.e., the eigenvalues are numerically exact. Comparing the 12D and 4D results for TRN(OH) one finds only marginal changes of the excitation frequencies; the ground state tunneling splitting is increased to $3.5\,\mathrm{cm}^{-1}$ (the change is about the accuracy of the present method). IR intensities change more strongly, but no qualitative changes occur. The finding suggest that, concerning the low lying energy levels, the 12D and the 4D model almost agree. Moreover, since the 4D results are numerically exact, it confirms the applicability of the method used for obtaining the 12D eigenvalues.

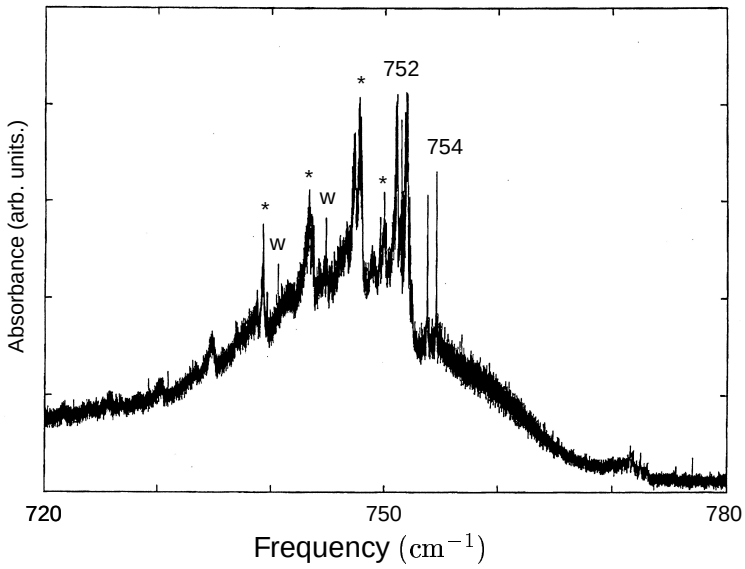

Figure 6.8: Experimental IR spectrum of TRN(OH) vapor at $T = 298.15\,K$ and $p = 1333\,\mathrm{Pa}$ near $750\,\mathrm{cm}^{-1}$ (taken from Ref. [40]). All values in cm^{-1}. Cold bands are marked by numbers; "*" marks hot bands and "w" marks transitions due to water vapor. The calculation centers on the peaks at $754\,\mathrm{cm}^{-1}$ (cf. Tab. 6.8 and Fig. 6.10); the experimental peak at $752\,\mathrm{cm}^{-1}$ is due to transitions into an out-of-plane mode.

Densities of low lying states obtained for the 4D model of TRN(OH) are shown in Fig. 6.7. Upon excitation the states corresponding to the reaction mode, $\Psi^{\pm}_{4^k}$, delocalize and spread towards the barrier region. This is in contrast to the states corresponding to the nascent tautomerization coordinate (cf. state $\Psi^{\pm}_{3^1}$); these states are almost orthogonal with respect to the reaction plane.

For the protonated species, TRN(OH), the present 12D model predicts two bright peaks in the IR spectrum at $749.3\,\mathrm{cm}^{-1}$ and $750\,\mathrm{cm}^{-1}$ (cf. Tab. 6.8). The experimental IR spectrum was measured with high resolution in the region between $960\,\mathrm{cm}^{-1}$ and $700\,\mathrm{cm}^{-1}$ by Redington *et al.* [40]. The spectral region near $750\,\mathrm{cm}^{-1}$ is shown in Fig. 6.8. Two transitions from the vibrational ground state were identified ("cold bands") by comparing spectra for different temperatures [40]. The peaks have rotational substructure. The doublet near $752\,\mathrm{cm}^{-1}$ was assigned to the H out-of-plane mode ($\mathcal{Y}^{(\mathrm{f})}_{26}$). The sharp doublet at $754\,\mathrm{cm}^{-1}$ has a splitting of $0.82\,\Delta_0^{(\mathrm{exp})} \approx 0.8\,\mathrm{cm}^{-1}$ and was assigned to correspond to the upper component of the transitions into the mode corresponding to the nascent tautomerization coordinate. This assignment was based on an empirical model [47]. However, the lower component was not found in the spectra of TRN(OH) vapor [40]. In a previous work, this component was assigned to a peak near $743\,\mathrm{cm}^{-1}$

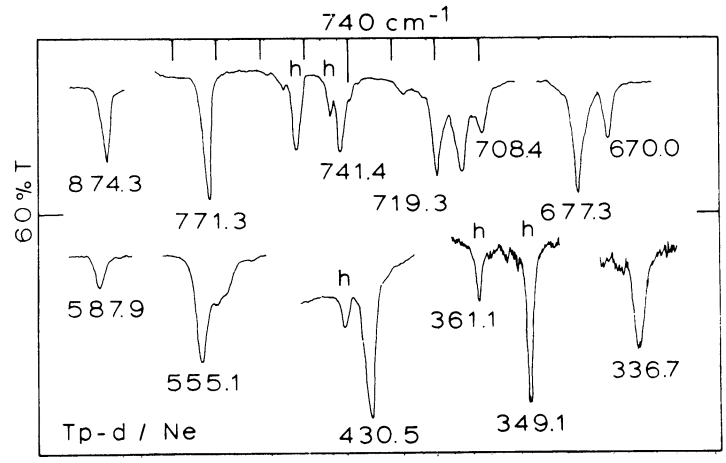

Figure 6.9: IR spectrum of Ne-Matrix isolated samples of the deuterated species TRN(OD) at $T = 5\,K$ for transitions below $900\,\mathrm{cm}^{-1}$ (taken from Ref. [166]). All values in cm^{-1}. Transition due to the protonated species TRN(OH) are marked by "h".

in Ne-matrix isolated TRN(OH).

A direct assignment of peaks calculated within the 12D model is hampered by the complicated substructure of the experimental spectrum. However, the coupling of mode $\mathcal{Y}_{28}^{(\mathrm{f})}$ to the tautomerization process appears to be insignifi cant, i.e., based on the present model this mode must be excluded from being a "nascent" tautomerization coordinate. In contrast, fundamentals and overtones corresponding to the reaction mode show a large mode-specifi cy of the tunneling splitting. The 12D model predicts a "doublet of doublet" (i.e., quartet) structure of the corresponding fundamental transitions (cf. Tab. 6.8). There are two broad peaks at, respectively, $361.1\,\mathrm{cm}^{-1}$ and $349.1\,\mathrm{cm}^{-1}$ in the experimental spectrum of Ne-matrix isolated samples of TRN(OH) [166]; these peaks are marked "h" in Fig. 6.9. The substructure of these peaks is presently unknown, but according to the present model they are candidates for a tunneling "quartet".

The effect of deuteration ("D-4" values in Tab. 6.8) signifi cantly decreases the splitting of the modes corresponding to the reaction mode. The ground state tunneling splitting of the deuterated species is reduced to $0.16\,\mathrm{cm}^{-1}$. The experimental ground state tunneling splitting was estimated by Jackman *et al.* [167] to be $\Delta_0^{(\mathrm{exp})}[TRN(OD)] \leq 0.17\,\mathrm{cm}^{-1}$. The measurement refers to TRN(OD) solved in $HCCl_3$; the value for gaseous TRN(OD) is presently unknown. The present theoretical value ($0.16\,\mathrm{cm}^{-1}$) for the 4D model of TRN(OD) appears to be consistent at least. In the Ne-matrix isolated IR spectrum of TRN(OD) there is only one broad peak at $336.7\,\mathrm{cm}^{-1}$ (cf. Fig. 6.9). This fi nding, too, is qualitatively consistent with the present theoretical prediction (cf. Tab. 6.8).

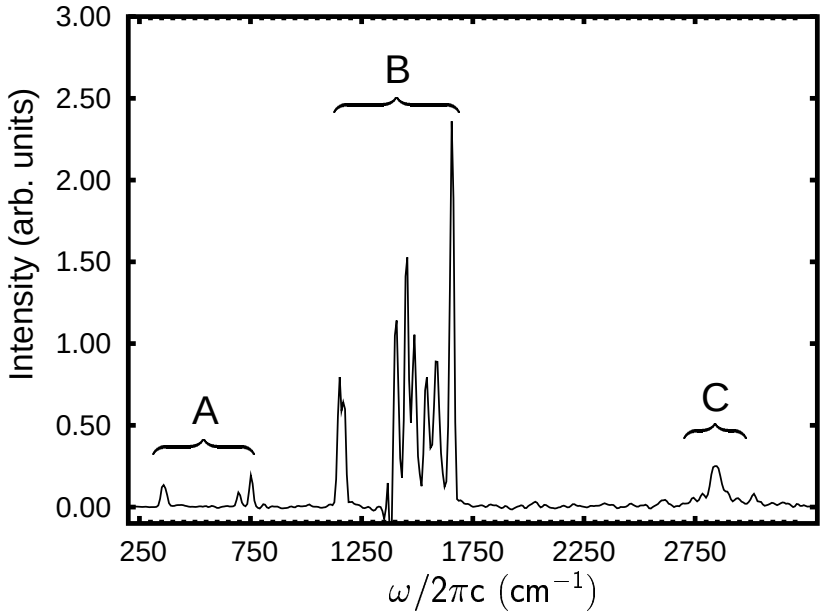

Figure 6.10: Overview of the computed IR spectrum of the 12D model of TRN(OH) at $T = 5\,K$.

6.2.4 The IR spectrum: $1000 - 1700\,\mathrm{cm}^{-1}$ range and OH stretch region

The remaining part of the spectrum can be obtained by Fourier transformation of the dipole-dipole autocorrelation function [168],

$$I^{\pm}(\omega) = \frac{4\pi\omega n_{\mathrm{mol}}}{3\hbar c} \sum_{\alpha=y,z} \mathrm{Re} \int_0^{\infty} dt\, W(t)\, e^{i\omega t}\, \langle \Psi_0^{\pm} | \hat{\mu}_{\alpha}(t) \hat{\mu}_{\alpha}(0) | \Psi_0^{\pm} \rangle, \qquad (6.12)$$

where n_{mol} is the number density of molecules, $\hat{\mu}_{\alpha}(t)$ is the dipole operator in the Heisenberg picture with space direction $\alpha = Y$ or Z (for in-plane transition), and $W(t) \sim \exp\left[-t^2/\tau^2\right]$ is a Gaussian window function to account for the limited time interval on which the correlation function is known. The parameter τ was $1\,ps$. The determination of the gerade and ungerade ground states was described above. The dipole-dipole correlation function was computed by performing a MCTDH propagation for a $3\ ps$ time interval. The dipole function was approximated according to Eq. (5.32)]. The primitive basis is given in Tab. 6.6; the number of SPF were 7 / 7 / 5 / 5 / 5 / 5. The maximum critical population for all four necessary propagations was $2.5 \cdot 10^{-3}$. This is similar to other applications of the MCTDH approach [150].

Figure 6.10 shows an overview of the computed IR spectrum at $T = 5\,K$. To this end, the spectra corresponding to transitions from the gerade and ungerade ground state, respectively, were weighted with the appropriate Boltzmann factor. The resolution is limited by the finite propagation time expressed by the window

	12D Model		Exp.	
state	$\varepsilon_{\mathbf{n}}/hc$	$\omega_k^{(12D)}/2\pi c$	[a]	[b]
2^1	1655	1662	1632	1634.2
3^1	low inten.	1655	1616	1616
4^1	1585	1593	1581.1	1581.1
5^1	1540	1535	1565.0	1565
6^1	1475, 1490[c]	1500	1498.9	1498.9
7^1	1450	1461	1431	1432.3
8^1	1405	1400	1413.6, 1315[d]	1413.6, 1317.8[d]
9^1	1150, 1170[c]	1271	1273.5	1272.3

[a] comparison of IR spectra obtained from vapor phase, solvated and rare gas matrix-isolated samples and MO computations [48];

[b] Ne matrix-isolated samples at $T = 5\,K$ [166];

[c] *resolved* tunneling doublets;

[d] RNM no. 8 has signifi cant overlap with two FNM (cf. Tab. 6.4)

Table 6.9: Fundamental transition energies (in cm^{-1}) of modes in the $1000 - 1700\,\mathrm{cm}^{-1}$ range. Values for the harmonic approximation to the 12D model of TRN(OH) ($\omega_k^{(12D)}$) and values ($\varepsilon_{\mathbf{n}}$) obtained by inspecting symmetry resolved Fourier transforms $I^{\pm}(\omega)$ [cf. Eq. (6.12)] with FWHM $\sim 9\,\mathrm{cm}^{-1}$ are compared with experimental observations. The displacement vectors of corresponding normal modes are depicted in Fig. 6.5.

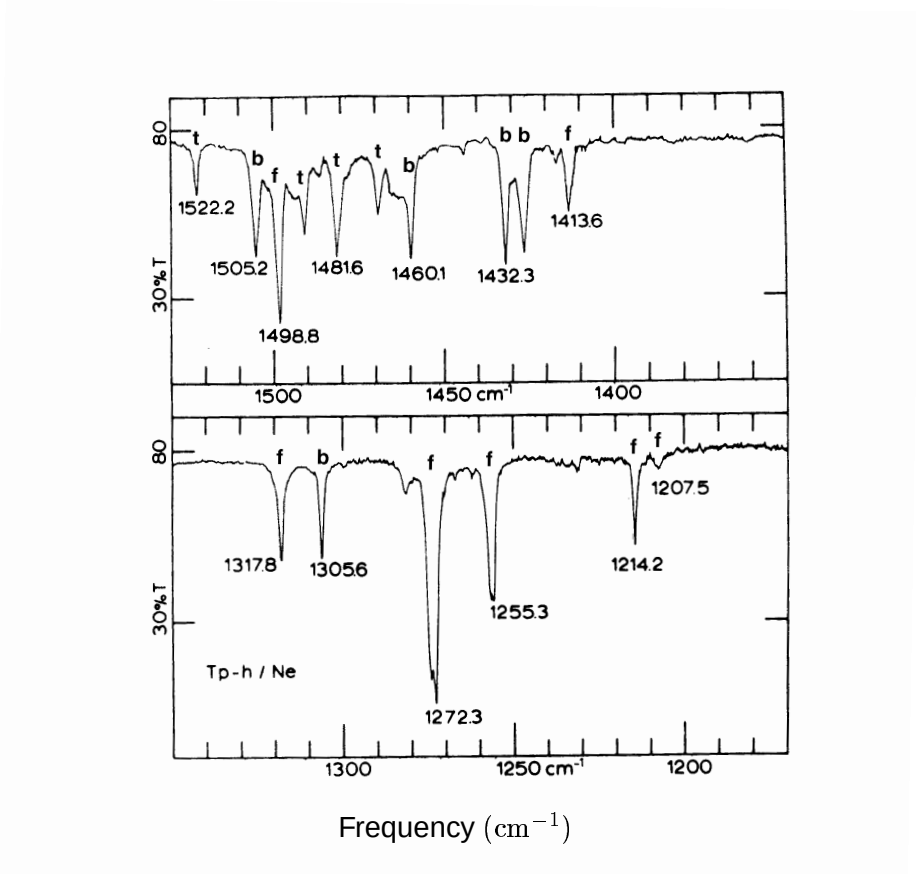

Figure 6.11: IR spectrum of Ne-matrix isolated samples of the protonated species TRN(OH) at $T = 5\,K$ between $1170 - 1530\,\mathrm{cm}^{-1}$ (taken from Ref. [166]). All values in cm^{-1}. Peaks marked with "f", "b", and "t" correspond to, respectively, fundamental transitions, binary combination transitions, and ternary combination transitions (assignment according to Ref. [48]).

parameter $\tau = 1\,ps$ corresponding to a full-width half-maximum (FWHM) of about $9\,\mathrm{cm}^{-1}$. Three regions are indicated by capitals, A, B, and C. Region A corresponds to Tab. 6.8 and was already discussed in Section 6.2.3. The RNM no. 2 to 9 reside in Region B; an assignment is given in Tab. 6.9. The values were obtained by inspecting $I^{+}(\omega)$ and $I^{-}(\omega)$ independently. The limited resolution permits the conclusion that the energy levels are only slightly perturbed as compared to the harmonic case (cf. Tab. 6.4). Harmonic and anharmonic values do reasonably well correspond to the assignment of experimental peaks. The left column of the experimental section corresponds to assigments that were made by comparison of IR spectra obtained from vapor phase, solvated, and rare gas matrix-isolated samples of TRN(OH) with MO computations [48]; the right column corresponds to Ne matrix-isolated samples.

In the theoretical spectrum, the tunneling splitting of states $\Psi^{\pm}_{6^1}$ and $\Psi^{\pm}_{9^1}$ (OH

bend) can be resolved to be about $15\,\mathrm{cm}^{-1}$ and $20\,\mathrm{cm}^{-1}$ (including the ground state splitting), respectively. The splitting of the other states is possibly unresolved. Note, the two corresponding RNM no. 6 and no. 9 have largest overlaps with the reaction plane among the modes in the energy range $1000 - 1700\,\mathrm{cm}^{-1}$ (cf. Tab. 6.4). However, the overlap of RNM no. 9 is artifically increased due to the reduced dimensionality. This is discussed below.

Experimentally, no tunneling splittings were assigned to mid-IR states [48]. However, there appear several peaks with significant intensity in the experimental spectra, and some of them were assigned to transitions into combination states of three (!) combined modes (ternary states) involving out-of-plane modes [48]. As an example, the spectral region between $1170 - 1530\,\mathrm{cm}^{-1}$ is shown in Fig. 6.11 (from Ref. [166]). Fundamental transitions ("f"), binary combination transitions ("b"), and ternary combination transitions ("t") according to Ref. [48] are indicated. The moderate anharmonic shift of the calculated values ($\varepsilon_{\mathbf{n}}$ in Tab. 6.9) as compared to the values obtained by harmonic approximation ($\omega_k^{(12D)}$) suggest a significantly lower intensity of transitions into combined states. (Recall, in the harmonic case the intensity of such transition vanishes identically.) The present calculation indicates that some of these peaks may be due to tunneling, instead.

State $\Psi_{9^1}^{\pm}$ corresponds to the OH bend. Experimentally, the OH bend was assigned to be at $1273.5\,\mathrm{cm}^{-1}$ and it has the largest IR intensity. A tunneling splitting of the OH bend was not assigned. The overlap of the RNM $\mathcal{Y}_9^{(12D)}$ with the FNM $\mathcal{Y}_{15}^{(\mathrm{f})}$, the "nominal" OH bend, is 0.72 (cf. Tab. 6.4), i.e., there is residual overlap with other full normal modes. The overlap of the RNM with the reaction plane is $(0.60, 0.11)$ [cf. Tab. 6.4]; the overlap of the FNM no. 15 with the reaction plane is $(0.31, 0.05)$. This means, the overlap of the FNM is reduced as compared to the RNM. In other words: the reduction procedure confines the OH bend more to the reaction plane. It is expected that this effect leads to an artificially reduced frequency and enhanced tunneling splitting of the OH bend. The true behavior of the OH bend cannot be predicted based on the present model.

Figure 6.12 shows the OH stretch Region C in more detail. The anharmonicity of the PES leads to the development of a broad structured band with a width of about $500\,\mathrm{cm}^{-1}$. The IR intensity of the OH stretch local mode is shared among various states. The individual states cannot be resolved due to the finite propagation time. There is a maximum of the gerade and ungerade transitions at, respectively, $(2836 \pm 4)\ cm^{-1}$ and $(2856 \pm 4)\ cm^{-1}$. A splitting of each single peak cannot be resolved. Compared to the $\mathcal{Y}_1^{(12D)}$ harmonic normal mode frequency of $3227\ cm^{-1}$ the OH stretch band maxima are red-shifted by about $380\ cm^{-1}$. The experimental OH stretch frequencies according to the assignment of Redington [48] are at $3121\ cm^{-1}$ and $3102\ cm^{-1}$; the assignment of Frost *et al.* [159]

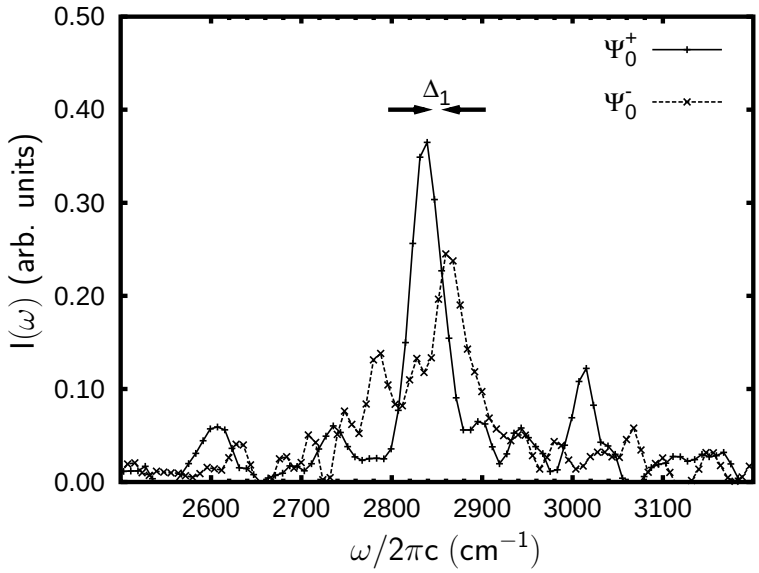

Figure 6.12: The OH stretch region computed for the 12D model of TRN(OH). Transitions with gerade and ungerade initial state are shown separately. Lines are drawn to guide the eye. The OH stretch tunneling splitting Δ_1 is indicated.

was 3134.9 cm^{-1} (from the gerade ground state). Thus, the theoretical prediction seems to be about 260 cm^{-1} too low. There are two effects that contribute to this underestimation of the OH stretch frequency: (i) Table 6.4 unveils that by going from the full-dimensional system to the 12D model the OH stretch frequency was decreased by 102 cm^{-1}, thus inclusion of more modes would shift the OH stretch of the 12D model to the blue. (ii) The quantum chemical barrier height of the present model is 2161 cm^{-1} obtained for the B3LYP/6-31+G(d) method. Barrier heights obtained by more sophisticated quantum chemical methods are shown in Tab. 6.1. For instance, Tautermann *et al.* [114] found a barrier of 2518 cm^{-1} by using the G3(MP2) method [162]. No rigorous convergence was achieved yet but the trend points toward a higher barrier as that obtained within the present quantum chemistry method. A higher barrier will largely effect those DOFs that are connected with the reaction plane and therefore shift the OH stretch further to the blue. However, the magnitude of that effect is diffi cult to judge. A simple linear scaling of the potential by the factor 1.17, to account for the expected higher barrier (say, 2518 cm^{-1}), would yield an approximate $\sqrt{1.17}$ shift of the frequencies, i.e., the computed OH stretch would shift to around 3078 cm^{-1}.

The computed OH-stretch tunneling splitting is tentatively assigned to be $\Delta_1 \approx (20 \pm 8)$ cm^{-1}. The nature of the underlying eigenstates is unknown, however. This issue is addressed in the following Section, Section 6.2.5. Moreover, it is necessary to investigate which mode contributes most (i.e., shows a large

mixing with the local OH stretch) to the development of the OH stretch band. This investigation of the coupling mechanism is addressed in Section 6.2.6.

Compared to the experimental value for the OH-stretch splitting, $\Delta_1^{(\mathrm{exp})} \approx 20\,\mathrm{cm}^{-1}$, of Redington *et al.* [48] there is a surprising agreement. However, note, the experimental assignment of the splitting is unclear. In particular, Frost *et al.* [159] did not observe a splitting and concluded that the "missing" component resides within unresolved absorption in a range of about $12\,\mathrm{cm}^{-1}$ to the red. Moreover, a slightly higher barrier would have a significant influence on the computed splitting. The present calculation confirms the experimental finding in so far, that a comparatively small OH-stretch splitting is predicted (in view of the excitation energy).

6.2.5 Semiclassical analysis

In the foregoing Section, the maxima corresponding to transitions from the gerade and ungerade ground state, respectively, were interpreted as the tunnel doublet of a perturbed OH stretch mode. However, the OH stretch transition is above the barrier, which is $2161\,\mathrm{cm}^{-1}$ for the present quantum chemical method [B3LYP/6-31+G(d)]. Barrier heights obtained within various other methods (cf. Tab. 6.1.) suggest that the conclusion is general. Moreover, the ZPE is $E_{\mathrm{ZPE}} = 8572\,\mathrm{cm}^{-1}$. Thus, the energy of classical ensembles corresponding to ground and excited states is above the barrier. This requires special treatment for the application of the Makri-Miller model (cf. Section 3.1.1). The present section proposes an interpretation of the observed effects in terms of *dynamical tunneling* [69, 169].

Consider an ensemble of trajectories with initial conditions generated by normal mode sampling (cf. Section 2.1.5). All trajectories are initially located in the right-hand well and the energy is scaled to the energy of a certain state of the 12D model. The ensemble averaged power spectrum (cf. Section 2.1.5) corresponding to the ground state and the first-excited OH stretch is shown in Fig. 6.13. The power spectrum requires a choice of an observable $Z(t)$; here the observable is

$$Z(t) \equiv P_{w_1} + P_{w_2} + P_{q_1}, \tag{6.13}$$

where P_{w_1} and P_{w_2} are the momenta corresponding to the two reaction coordinates w_1 and w_2 and P_{q_1} is the momentum corresponding to the coordinate $q_1 \equiv Q_4$. (Any other choice is equally well suited, but may differ in peak intensities.) A symplectical integrator of fifth-order with fixed step-size of $0.2\,\mathrm{fs}$ was used and the propagation time was $14.5\,ps$. The peaks (or bands) correspond to the fundamental frequencies of the system and linear combinations thereof. The OH stretch region is characterized by a broad band. A pronounced broadening is also found

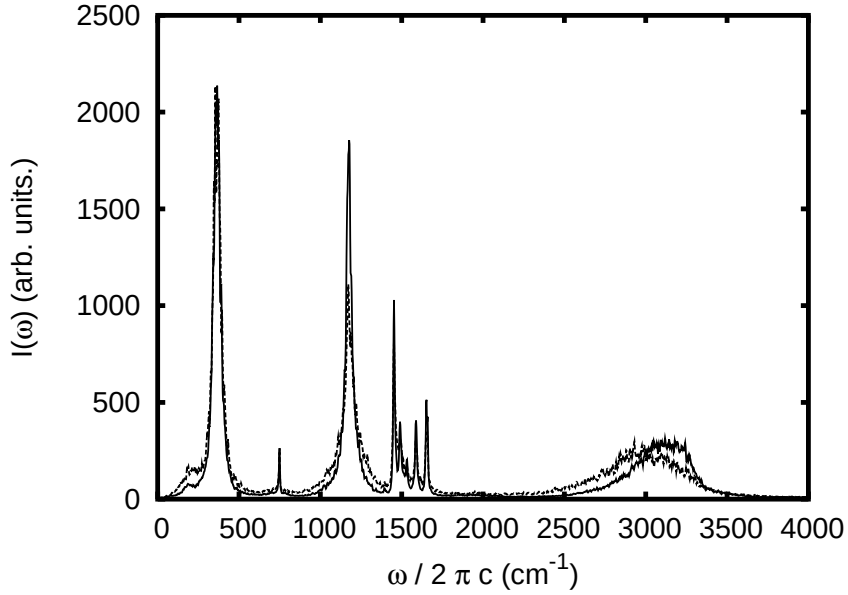

Figure 6.13: The 12D model of TRN(OH): Power spectra for ensembles of 100 trajectories corresponding to the ground state (solid) and the first-excited OH stretch (dashed). The spectra are normalized. The initial conditions were obtained by normal mode sampling. The underlying observable $Z(t)$ is defined in Eq. 6.13.

for peaks corresponding to the reaction mode and the OH bend, respectively. The appearance of broad peaks indicates that the classical dynamics is of the mixed type, i.e., regular and irregular trajectories exist close to each other. Comparing the two spectra (the spectra are normalized), a marginally pronounced broadening is found for the ensemble of the first-excited OH stretch and one observes a shift of the band maximum from about $3100\,\mathrm{cm}^{-1}$ (ground state) to about $2900\,\mathrm{cm}^{-1}$ (first excited OH stretch). This shift is reminicent of Fig. 6.12, where the band maximum is at about $2840\,\mathrm{cm}^{-1}$.

The ground state energy is $8516\ \mathrm{cm}^{-1}$ with respect to the minima. Thus, compared to the barrier height of $2161\ \mathrm{cm}^{-1}$ the ground state level is $6355\ \mathrm{cm}^{-1}$ above the barrier, i.e., there is no barrier preventing the trajectories of the considered ensembles from reaching the other (left) well. Figure 6.14 shows the fraction of trajectories $P_R(t)$ that are in the right well after time t for ensembles of 1000 trajectories corresponding to the considered states. For the ground state ensemble there is a slight decay; after 450 fs the fraction has dropped to about 90 %. For the first excited OH stretch there is a comparatively fast equilibration (equal distribution over both wells) of the ensemble within about 100 fs.

The numerical observations may be explained, when assuming the existence of right (and left) localized invariant tori (cf. Section 2.1.1). These invariant

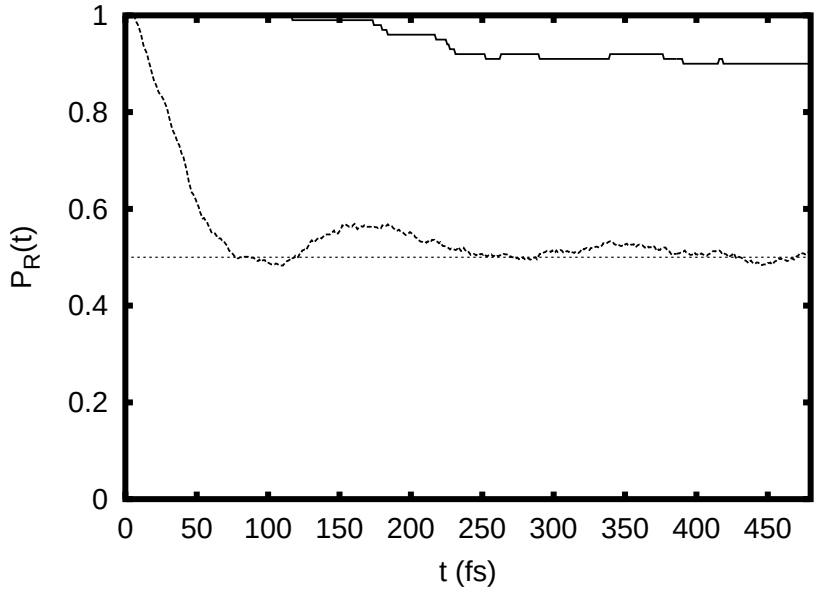

Figure 6.14: The 12D model of TRN(OH): Classical survival probability $P_R(t)$ for the fraction of trajectories that are in the right-hand well after propagation time t. Results for a ground state (solid) ensemble and the first-excited OH stretch (dashed) are shown.

tori are regular regions of phase space embedded in an otherwise irregular phase space [49]. A certain invariant torus corresponds to the ground state and the first excited OH stretch. The normal mode sampling method generates trajectories that are close to the particular invariant tori [99]; some trajectories may also be on these tori. Trajectories that are close to a torus but in the irregular region of phase space stay for a certain time close to the torus but then wander away [64] and eventually cross the symmetry line leading to a equilibration of $P_R(t)$. The irregular region of phase space increases with increasing energy. The power spectrum of the considered scenario would look like the one found in Fig. 6.13.

If there is a right localized regular regions of phase space, then there is always a symmetrically equivalent left localized regular region of phase space and vice versa [170]; both regions are mapped onto each other by the symmetry transform T (for a Cartesian Hamiltonian; cf. Sec. 2.2.1). The two corresponding energetically degenerate left and right localized semiclassical wave functions form zero-order states for quantum mechanics. In quantum mechanics, the gerade and ungerade superposition of both zero-order states leads to split energy levels [170, 69, 169]; since the splitting is a quantum effect it is due to a classical forbidden process, namely tunneling (cf. Section 2.2.2).

On the opposite, all irregular regions of phase space are expected to be invariant with respect to T, because Arnold diffusion prevents a trapping of trajectories

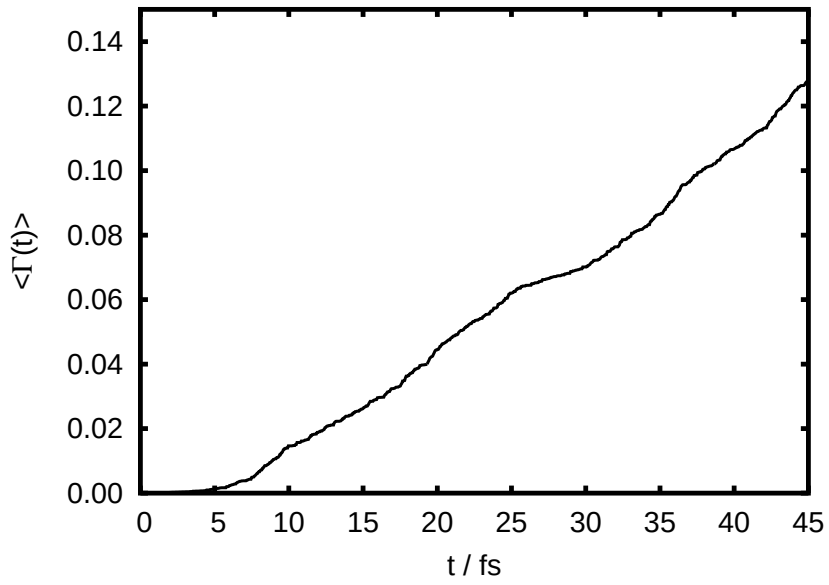

Figure 6.15: The 12D model of TRN(OH): Cumulated tunneling probability $\langle\Gamma(t)\rangle$ for an ensemble of 2000 trajectories corresponding to the first-excited OH stretch. The maximum propagation time was $T_{\max} = 48\,\mathrm{fs}$. The deviation from linearity is due to the approximate nature of the normal mode sampling method.

[64]. As a consequence, there are no irregular regions with tunneling splittings [170]. Thus, the appearance of a tunneling splitting suggests that there are corresponding zero-order states localized on regular regions of phase space [170, 171].

The low lying states of the 12D (and 4D) model of TRN(OH) appear in split pairs (cf. Tab. 6.8). Visual inspection of the states of the 4D model (cf. Fig. 6.7) unveils that these states are regular. The same is anticipated for the 12D model. If these states were localized on a delocalized invariant torus (i.e., a torus that is invariant with respect to T), there would be a local maximum of the density along the symmetry surface for a gerade state, because the momentum at the symmetry line is smaller than at the minima. This consideration supports the assumption that there are right and left localized invariant tori corresponding to the low lying levels shown in Tab. 6.8. The absence of an energy barrier implies, that the splitting is due to dynamical tunneling [69, 169]. Moreover, the power spectrum suggests, that the ensembles generated by normal mode sampling with energy rescaling are reasonable approximations to the invariant tori. This justifies the application of the semiclassical Makri-Miller model (cf. Section 3.1.1) in order to calculate semiclassical tunneling splittings for the low lying states. On the other hand, no such conclusions can be made for the OH stretch, because the shape of the wave function is not known. Tentatively, the Makri-Miller model is also applied to the OH stretch.

state	gs$^{(a)}$	1^1	2^1	3^1	4^1	5^1	6^1
$\Delta_{\mathbf{n}}^{(\mathrm{QM})}$	2.7	$\sim$ 20	(b)	(b)	(b)	(b)	$\sim$ 15
$\Delta_{\mathbf{n}}^{(\mathrm{MM})}$	6	32	6	7	6	6	8

state	7^1	8^1	9^1	10^1	11^1	12^1	12^2
$\Delta_{\mathbf{n}}^{(\mathrm{QM})}$	(b)	(b)	$\sim$ 20	2	3	14	40
$\Delta_{\mathbf{n}}^{(\mathrm{MM})}$	6	5	17	6	6	19	27

$^{(a)}$ ground state; $^{(b)}$ splitting $< 9\,\mathrm{cm}^{-1}$

Table 6.10: Mode-specific tunneling splittings (in cm^{-1}) obtained for the 12D model of TRN(OH): Quantum mechanical (QM) values $\Delta_{\mathbf{n}}^{(\mathrm{QM})}$ and values $\Delta_{\mathbf{n}}^{(\mathrm{MM})}$ obtained by the Makri-Miller method with a modified sampling scheme (see text). The QM values are compiled from Tab. 6.8, Tab. 6.9, and Fig. 6.12.

The Makri-Miller model was not applied directly to the normal mode sampling ensembles: those trajectories, that crossed the symmetry line during a fixed given maximum propagation time $T_{\max} = 48\,\mathrm{fs}$ were discarded. Thus, the ensembles consisted only of trajectories that are localized in the right-hand well for at least time $T_{\max}$. The larger $T_{\max}$, the closer are the trajectories initially to invariant tori. The tunneling direction $\mathbf{d}$ was choosen to coincide with the straight line connecting the two minima $\mathbf{w}_1$. Recall, the minima are at $(\pm w_1^{(\min)}, w_2^{(\min)}, \mathbf{q} = 0)$. Thus, concerning both, the symmetric *and* anti-symmetric modes, the present choice of $\mathbf{d}$ is consistent with the original proposal of Makri and Miller [29] (cf. Fig. 3.1a and 3.1c).

The cumulated tunneling probability $\langle \Gamma(t) \rangle$ corresponding to the first-excited OH stretch is shown in Fig. 6.15. Note, there are deviations from linearity, because the ensembles do not exactly correspond to the associated invariant torus [99]. The slopes were determined by using linear regression of the computed data, i.e., a least squares fit of a function $A \cdot x + B$. The deviation from linearity leads to a non-vanishing B in the present case. This fitting procedure is reasonable, because all points are equivalent. (The time origin is arbitrary.)

The semiclassical tunneling splittings are given in Tab. 6.10. The general findings are rather similar to those already reported in Chapter 3: the semiclassical tunneling splittings agree with respect to exponential accuracy. The enhancement of the tunneling splitting upon excitation of the reaction mode is also reproduced qualitatively. More important is the result concerning the semiclassical OH stretch tunneling splitting. The magnitude clearly agrees with the exact quantum mechanical value. This observation suggests that the OH stretch is split by a classical forbidden process.

6.2.6 Coupling mechanism

This Section addresses the coupling mechanism that leads to the broad structured absorption in the OH stretch region of the 12D model (cf. Sec. 6.2.3). In harmonic approximation (i.e., without any kind of mode coupling and anharmonicity) there is only one state above $2000\ \mathrm{cm}^{-1}$ that can be reached by an IR transition from the ground state: the state corresponding to the fundamental excitation of the OH stretch local mode. Thus, the OH stretch band must be due to couplings of the local OH stretch with other modes. The primary goal is to identify the modes with strongest coupling to the OH stretch.

The selection of relevant modes of the 12D model in Section 6.2.2 was motivated by the first-order perturbation theory expression Eq. (6.4); modes corresponding to combination states in a $\pm 200\ \mathrm{cm}^{-1}$ range were included (width of the experimental OH stretch region). In the present Section the choice of relevant modes is scrutinized in view of the full anharmonicity of the Hamiltonian.

The states $\Psi_{\mathbf{n}}^{(0,R)}$ ($\Psi_{\mathbf{n}}^{(0,L)}$) corresponding to the harmonic approximation to the right (left) minimum form a complete basis. Moreover, in the absence of anharmonic couplings, these states would be the eigenstates of the Hamiltonian. For this reason, the harmonic states serve as reference, i.e., in the following the coupling among *harmonic* modes is investigated. This choice of reference is in accord with the usual interpretation of IR spectra, that is based on the harmonic approximation (for instance, see Ref. [48]).

The harmonic Hamiltonian for the right-hand modes reads [III],

$$\hat{H}_0^{(R)} = \sum_j \hbar\omega_j \left(\hat{n}_j^{(R)} + \frac{1}{2} \right), \tag{6.14}$$

where $\hat{n}_j^{(R)}$ is the number operator of harmonic mode j located on the right-hand side. Likewise, one can define $\hat{H}_0^{(L)}$ for the left side, where in Eq. (6.14) "R" is replaced by "L". Here, the expectation value of $\hat{H}_0^{(R)}$ is defined by the real part of the half-space integral [III],

$$\langle \hat{H}_0^{(R)} \rangle_R = Re \int_{x>0} d\mathbf{r}\ \Psi^* \hat{H}_0^{(R)} \Psi. \tag{6.15}$$

Equivalently, $\langle \hat{H}_0^{(L)} \rangle_L$ can be defined for the left half-space. The consideration of right and left expectation values is necessary, because otherwise the population of, for instance, a right-localized OH stretch would correspond to a very high population of various left-localized modes.

The expectation value of the *full* Hamiltonian $\hat{H}$ can be divided according to,

$$\langle \hat{H} \rangle = \langle \hat{H}_0^{(R)} \rangle_R + \langle \hat{H}_0^{(L)} \rangle_L + \langle \hat{H}_A \rangle, \tag{6.16}$$

where the Hamiltonian $\hat{H}_A$ contains the anharmonic part of the full Hamiltonian. The contribution of $\hat{H}_A$ is expected to be especially large in the barrier region. In Eq. (6.14) together with Eq. (6.15) one can identify the energy expectation value without zero point energy of right mode j, as

$$\langle \hat{E}_j^{(R)} \rangle_R = \hbar\omega_j \langle \hat{n}_j^{(R)} \rangle_R \tag{6.17}$$

and analogous for the left energy $\langle \hat{E}_j^{(L)} \rangle_L$.

Consider the state corresponding to the single excited local OH stretch mode localized at the right-hand side: $\Psi_{1^1}^{(0,R)}$. (The notation was introduced in Section 6.2.3.) The time evolution of this state with respect to the full Hamiltonian $\hat{H}$ leads to preferential energy flow in those modes, that are coupled to the local OH stretch mode. Thus, the energy flow pattern yields information about the coupling among modes.

The actual time-evolution of the intial state $\Psi_{1^1}^{(0,R)}$ was performed using the MCTDH method. The primitive basis and mode combination is given in Tab. 6.6. The number of SPF per combined mode was 9 / 8 / 4 / 4 / 4 / 4. The propagation interval was 500 fs and the maximum critical population was $4 \cdot 10^{-2}$.

Figure 6.16a shows the probability for finding the hydrogen in a right-hand configuration [i.e., the expectation value of $P_R(t) = \langle \Psi(t) | \Psi(t) \rangle_R$]. The delocalization of the time-evolved state among the two sides is very fast; after 100 fs the fluctuations around equilibrium are less than 0.1. Also shown in Fig. 6.16a are results obtained for a classical ensemble (cf. Fig. 6.14); the ensemble was generated by normal mode sampling with energy rescaling. Fluctuations around equilibrium are less pronounced for the classical ensemble.

The total energy $E_{\mathrm{tot}} = \langle \Psi(t) | \hat{H} | \Psi(t) \rangle$ is constant with respect to time. It can be divided according to (cf. Eq. 6.16),

$$E_{\mathrm{tot}} = E_{\mathrm{ZPE}} + E_{R+L}(t) + E_A(t) = \mathrm{const}, \tag{6.18}$$

where $E_{\mathrm{ZPE}} = 8572\ \mathrm{cm}^{-1}$ is the constant zero-point energy (ZPE) of the harmonic modes, $E_{R+L}(t)$ is the sum of the energy (without ZPE) in all harmonic modes,

$$E_{R+L}(t) = \sum_j \left(\langle \hat{E}_j^{(R)} \rangle_R + \langle \hat{E}_j^{(L)} \rangle_L \right), \tag{6.19}$$

and $E_A(t) = \langle \Psi(t) | \hat{H}_A | \Psi(t) \rangle$ is the energy of the anharmonic part of the Hamiltonian. Additionally to the energy that is bound in certain harmonic modes there is also some energy bound in the *interaction* among harmonic modes. For the present case this interaction is attractive, i.e., the anharmonic contribution is negative indicating a lowering of mode energies due to the anharmonicity of the PES.

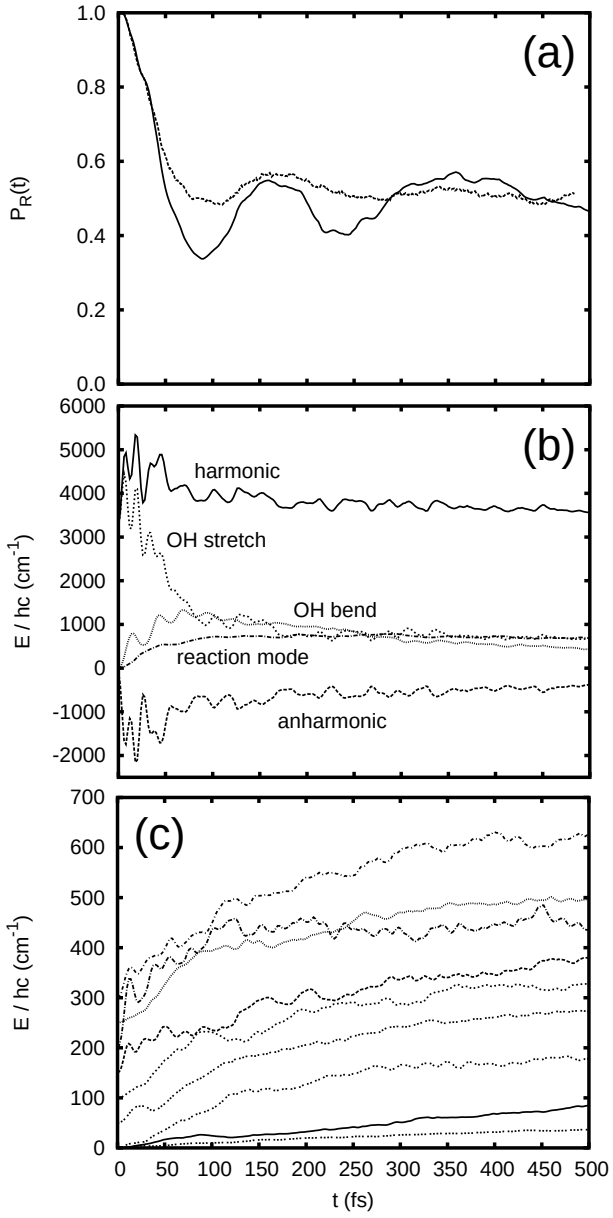

Figure 6.16: Results for the 12D model of TRN(OH). The initial wave packet is the harmonic oscillator state corresponding to a singly excited OH stretch. (a) Time-evolution of the expectation value $P_R(t) = \langle\Psi(t)|\Psi(t)\rangle_R$. (b) Energy flow for specifi c modes (indicated) as well as sums of the harmonic $E_{R+L}(t)$ and anharmonic $E_A(t)$ contributions [cf. Eq. (6.18)]. (c) Same as before, but for remaining modes (from bottom to top): mode no. 11, 2, 8, 10, 4, 3, 6, 5, and 7. The curves are shifted by steps of $50\,\mathrm{cm}^{-1}$ (except for curves corresponding to mode no. 11, 2, and 8); the energy is $E = 0$ at $t = 0$ for all curves.

The initial harmonic energy is $E_{R+L}(t = 0) = 3227\ \mathrm{cm}^{-1}$, because the inital state is the (right-localized) OH stretch. The initial anharmonic energy is $E_A(t = 0) = -46\ \mathrm{cm}^{-1}$. The time-evolution of $E_{R+L}(t)$ is shown in Fig. 6.16b (indicated as "harmonic"). The equilibration process (cf. Fig. 6.16a) is accompanied by pronounced fluctuation of $E_{R+L}(t)$. After about 50 fs the fluctuation amplitude signifi cantly decreases and the curve approaches a plateau above $3500\ \mathrm{cm}^{-1}$. Thus, roughly there is a $250\ \mathrm{cm}^{-1}$ energy contribution flowing from the anharmonic part into the harmonic part. Compared to the initial harmonic energy this is less than 8 %. This observation justifi es the use of harmonic modes in order to study the coupling.

The energy flow of individual modes is also shown in Fig. 6.16 [panel (b) and (c)]. In view of the fast equilibration, for each mode j the sum of left and right contribution, i.e., $\langle \hat{E}_j^{(R)} \rangle_R + \langle \hat{E}_j^{(L)} \rangle_L$, is shown. The OH stretch energy decays to a plateau above $600\ \mathrm{cm}^{-1}$ within roughly 200 fs. A single exponential fi t of a function $f(t) = \omega_1^{(12D)} \left(A + (1 - A)\, e^{-t/\tau}\right)$ to the curve leads to a life-time of $\tau \approx 77$ fs. For times smaller than 50 fs there are oscillations with considerable amplitude and period of about $T \approx 12$ fs; this oscillation period correspond to a frequency of about $2800\ \mathrm{cm}^{-1}$. The oscillations are due to the fact, that the OH stretch is an anharmonic mode. (For instance, the same behavior would be found, when applying the defi nition of $E_1^{(R)}$ to a Morse oscillator.)

The initial OH stretch energy dissipates into the remaining modes. After 500 fs the energy contribution of the OH stretch, OH bend and reaction mode is, respectively, $650\,\mathrm{cm}^{-1}$, $440\,\mathrm{cm}^{-1}$, and $680\,\mathrm{cm}^{-1}$ (cf. Fig. 6.16b), where the slope of the former two is almost zero, while the slope of the OH bend is negative. The other modes acquire between $40\,\mathrm{cm}^{-1}$ and $350\,\mathrm{cm}^{-1}$ energy in the same time period (cf. Fig. 6.16c). The OH bend curve has a maximum of $1270\,\mathrm{cm}^{-1}$ (about one quantum) at 94 fs and shows pronounced fluctuations during the fi rst 150 fs. The energy content of the reaction mode is about $720\,\mathrm{cm}^{-1}$ after 100 fs; the energy content of the remaining modes less than $250\,\mathrm{cm}^{-1}$ after 100 fs. The mean rate of energy flow is therefore signifi cantly larger for the OH bend and reaction modes than for the remaining modes. Yet the energy content of the remaining modes is signifi cant.

Unlike the absolute energy content of each individual mode, which will equilibrate to the same value, the mean rate of energy flow vs. time is a measure for the coupling strength. It is not surprising that there is a signifi cant coupling of the OH stretch to the OH bend and reaction mode because these three modes have marked overlaps with the reaction plane (cf. Tab. 6.4). However, a particular important fi nding of the present section concerns the signifi cant coupling of the remaining modes to the OH stretch.

One may interpret the local OH stretch harmonic state as a *bright* state as is usual in the context of intramolecular vibrational energy redistribution (IVR) [21, 20, 4]. A similar approach was used in a theoretical study of the IVR in benzene [172]. This interpretation is suggested by the fact, that the mean energy of the singly excited harmonic OH stretch is almost unchanged as compared to the harmonic case; the anharmonic energy contribution, $E_A(t=0)$, is only $-46\,\mathrm{cm}^{-1}$. Therefore, the present initial state is a well defined zero-order state [21, 20]. Furthermore, since the harmonic ground state is very similar to the corresponding superpositions of gerade und ungerade ground states the oscillator strength for transitions into the harmonic OH stretch is large, while it is very small for transitions into combination states involving the OH stretch. This is the definition of a bright state. However, the IR transitions induced by a time-dependent laser field would probably excite a different bright state, yielding energy redistribution and time scales.

Assuming the present initial state is a bright state, then there are two channels for the decay of the OH stretch. Channel (1) is the direct dissipation of energy into the remaining modes and channel (2) is a dissipation via the OH bend, which has a maximum at $94\,\mathrm{fs}$ and slowly decays afterwards. These findings are reminicent of the cascaded energy redistribution in phthalic acid monomethyl ester [173], where the energy redistribution of the OH stretch (experimental lifetime $220\,\mathrm{fs}$) was found to originate from a cascaded process involving the OH bend mode. However, the decay times should be compared with caution, since the initial states are different.

6.2.7 Chlorine substitution

For TRN(OH) it was found that tunneling is significantly promoted by exciting the reaction mode, where the reaction mode is mainly a superposition of the two in-plane modes with lowest frequency (cf. Fig. 6.4). A perturbation may alter the tautomerization mechanism. Such a perturbation is introduced, e.g., by a symmetrical substitution of hydrogen by chlorine ^{35}Cl at the C_3 and C_7 position of tropolone (cf. Fig. 6.17a). The name of this compound is 3,7-dichlorotropolone [DCTRN(OH)].

The effect of halogen atom substitution on the mode specific tunneling splittings was investigated by Sekiya *et al.* [158] for the first electronically excited state S_1 of symmetrically substituted tropolones. Concerning the compound DCTRN(OH), it was found that Δ_0^*, that is, the absolute difference between the ground state tunneling splittings of S_0 and S_1, was significantly increased to $45\ cm^{-1}$ in DCTRN(OH) compared to $19\ cm^{-1}$ in TRN(OH). Furthermore it

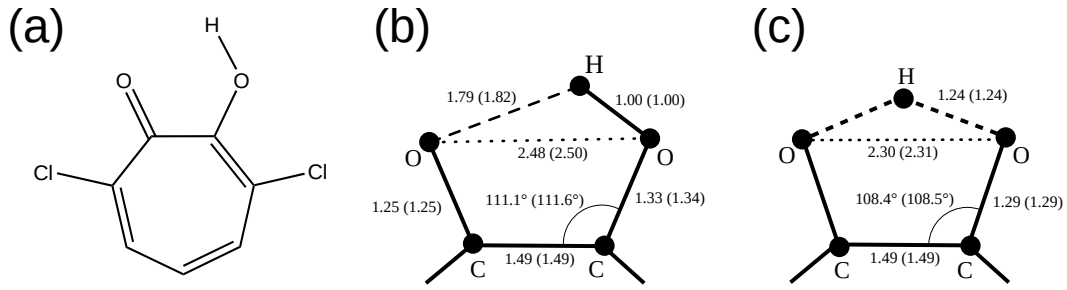

Figure 6.17: (a) Chemical structure of 3,7-dichlorotropolone [DCTRN(OH)]. (b) Minimum geometry of the OCCO-H fragment of DCTRN(OH) [B3LYP/6-31+G(d)]. Bond lengths (in Å) and one angle (in degree) are given. Values for TRN(OH) in parenthesis. (c) Same as (a) but for the saddle point geometry of the OCCO-H fragment of DCTRN(OH).

was found that upon excitation of the $CO\cdots COH$ bending mode the splittings are $30\ cm^{-1}$ and $53\ cm^{-1}$ for TRN(OH) and DCTRN(OH), respectively. Here, the relative change of the splitting was more pronounced for the parent compound. The results are not directly applicable to the electronically ground state, because mode characters and barriers are likely to differ signifi cantly. However, the experimental observations suggest that there may be a considerable change in the tautomerization mechanism upon chlorine substitution.

In this Section the differences of the tautomerization in TRN(OH) and DCTRN(OH) is analyzed. The analysis is analogous to the case of TRN and based on the CRP approach. The quantum chemical calculations (potential energies, gradients, Hessians, and IRP) are based on the DFT method (B3LYP functional) and the 6-31+G(d) basis set. The quantum chemical barrier $\Delta E_{\mp} = 2115\ cm^{-1}$ of DCTRN(OH) is virtually unchanged as compared to the parent compound where it is $2161\ cm^{-1}$. The same is true for the geometry of the OCCO-H fragment which is shown in Fig. 6.17 for, respectively, the minimum geometry (panel b) and the saddle point geometry (panel c). Especially the geometrical parameters of the hydrogen bond, e.g., the O-O distance and the two H-O distances, only differ by few 1/100 Å. The passiveness of the hydrogen bond upon chlorine substitution is also reflected by normal modes that are localized at the hydrogen bond: Normal mode frequencies of the OH stretch ($3317\,\mathrm{cm}^{-1}$) and H out-of-plane ($825\,\mathrm{cm}^{-1}$) modes only slightly differ from the corresponding values of the parent compound (cf. Tab. 6.2). The OH bend ($1428\,\mathrm{cm}^{-1}$) is blue-shifted by about $100\,\mathrm{cm}^{-1}$, which can be attributed to the larger mixing with CH bends of the ring.

The characters and frequencies of the remaining normal modes change more strongly because these modes do involve displacements of ring atoms. The chemi-

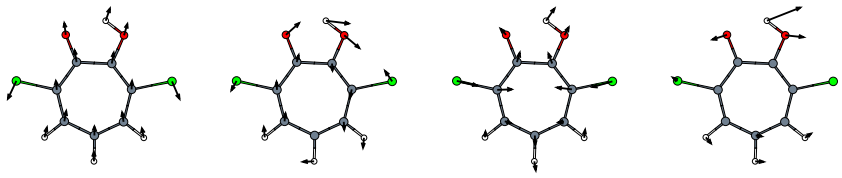

Figure 6.18: Full normal modes of DCTRN(OH): The three weakest in-plane normal modes $\mathcal{Y}_{36}^{(f)}$, $\mathcal{Y}_{35}^{(f)}$, $\mathcal{Y}_{33}^{(f)}$ (*chlorine modes*), and the $CO\cdots COH$-bending mode $\mathcal{Y}_{31}^{(f)}$. Frequencies are indicated and the dimensionless value δ measures the change of the hydrogen bond induced by each mode [cf. Eq. (6.2)].

cal effect of chlorine - as a more electronegative element than hydrogen - is to pull electron density out of the ring. This leads to a significant change of force constants. Furthermore, the comparatively large chlorine mass leads to several modes below 300 cm^{-1}. The three in-plane modes with lowest frequency are shown in Fig. 6.18 together with the $CO\cdots COH$-bending mode. The character of the first mode no. 36 is a down (up) shift of the chlorines accompanied by an opposite shift of the seven-membered ring and the OCCO-H fragment in order to keep the center of mass fixed. Mode no. 35 involves a rotation of the chlorines accompanied by a counter rotation of the remaining atoms, and mode no. 33 is a squeezing mode of the molecule. The change in hydrogen bond geometry induced by these three modes is rather insignificant as compared to, e.g., the $CO\cdots COH$-bending mode, which is also shown in Fig. 6.18. This statement can be quantified by the dimensionless value δ [cf. Eq. (6.2)] that is given in the same figure.

The RMS atom displacement along the IRP [cf. Eq. (5.4)] is below $0.025\,\mathring{A}$; the maximum energy difference between the IRP and its projection onto the reaction plane is below $190\,\mathrm{cm}^{-1}$ [B3LYP/6-31+G(d) level of theory]. Thus, the application of the CRP approach is reasonable. A minimal 3D model is obtained by treating only the OH stretch normal mode as relevant. Recall, the reaction plane DOF are included by definition. Overlaps and frequencies of reduced and full normal modes are given in Tab. 6.11.

For TRN(OH) the weakest in-plane modes no. 36 and 37 have the two largest δ values of, respectively, 45 and 44 (cf. Tab. 6.2), and the reaction mode is a superposition of these modes. For DCTRN(OH), the stable limit theorem states that the IRP approaches the minimum along the weakest in-plane mode, mode no. 36 (cf. Fig. 6.18). However, the theorem is valid only in the immediate vicinity of the minimum and the δ-value of FNM no. 36 is significantly lower than the

full			3D				
no.	$\omega_k^{(\mathrm{f})}/2\pi c$	Inten.	overlap	mode	$\omega_k^{(\mathrm{3D})}/2\pi c$	w_1	w_2
1	3317	123	0.91	$\mathcal{Y}_1^{(\mathrm{3D})}$	3045	0.64	0.32
8	1514	58	0.30				
10	1428	333	0.43	$\mathcal{Y}_2{}^{(\mathrm{3D})}$	1328	0.68	0.16
11	1405	172	0.43				
29	469	1.3	0.30				
31	435	21	0.83	$\mathcal{Y}_3{}^{(\mathrm{3D})}$	430	0.35	0.93
33	275	0.8	0.37				

Table 6.11: Comparison of normal modes of the full-dimensional system ("full") with the reduced normal modes of the 3D model ("3D") for DCTRN(OH). Frequencies ω_k (in cm^{-1}), IR intensities ("Inten."; in km/mol), overlaps of the reduced normal modes with full normal modes [cf. Eq. (5.36)], and overlaps with the reaction plane are given (cf. Tab. 6.4).

δ-value of FNM no. 31, which has the largest δ-value among all FNM of DCTRN(OH). Moreover, Table 6.11 unveils that the RNM with lowest frequency has a pronounced overlap with FNM no. 31; this FNM is very similar to the reaction mode of TRN(OH) (cf. RNM no. 12 in Fig. 6.5). A diagonalization (using the Lanczos algorithm) of the 3D Hamiltonian of DCTRN(OH) [B3LYP/6-31+G(d)] yields a ground state tunneling splitting of $\Delta_0 = 4.6\,\mathrm{cm}^{-1}$; the gerade (ungerade) energy levels corresponding to the fundamental and first overtone state of RNM no. 3 are $364\,(393)\,\mathrm{cm}^{-1}$ and $697\,(774)\,\mathrm{cm}^{-1}$, i.e., the tunneling splittings are, respectively, $29\,\mathrm{cm}^{-1} = 6.3\,\Delta_0$ and $77\,\mathrm{cm}^{-1} = 16.7\,\Delta_0$. For TRN(OH) the enhancement was, respectively, 5.2 and 17.4 times the ground state splitting, i.e., the relative enhancement of the tunneling splitting is similar to TRN(OH). (Unlike the suggestion of the experimental finding concerning the excited electronic state [158].) The consideration of the anharmonic PES is essential for the present finding. It is found that the reaction modes of TRN(OH) and DCTRN(OH) have similar frequency, show similar mode-specificy upon excitation, and have similar displacement vectors. Thus, concerning the reaction mode, the present investigation unveils that the tautomerization mechanism of TRN(OH) and DCTRN(OH) is similar.